Jonas Lyng-Jørgensen

Investigating the Magnetic Characteristics of Oxidized $Ni_{80}Fe_{20}$ Structures and the Integrity of Al Capping Layers Used as an Oxidation Barrier

Master's thesis in Nanotechnology
Supervisor: Erik Folven
Co-supervisor: Jakob Vinje & Anders Strømberg
June 2022

Master's thesis

NTNU
Kunnskap for en bedre verden

Jonas Lyng-Jørgensen

Investigating the Magnetic Characteristics of Oxidized Ni$_{80}$Fe$_{20}$ Structures and the Integrity of Al Capping Layers Used as an Oxidation Barrier

Master's thesis in Nanotechnology
Supervisor: Erik Folven
Co-supervisor: Jakob Vinje & Anders Strømberg
June 2022

Norwegian University of Science and Technology
Faculty of Information Technology and Electrical Engineering
Department of Electronic Systems

NTNU
Norwegian University of
Science and Technology

Abstract

Artificial spin ices (ASI) are metamaterials comprised of nanosized ferromagnets arranged at various geometries, leading to exotic magnetic behavior, and represent potential candidates for use in low-energy unconventional computing. An integral part of developing this novel technology is ensuring the long-term stability of the magnetic structures to guarantee non-volatile information storage. Typically the nanomagnets comprising the ASIs are made of the nickel-iron alloy $Ni_{80}Fe_{20}$ (Permalloy) with an additional Al capping layer. Knowing that Permalloy forms oxides belonging to various magnetic classes, the effects of oxidation on the magnetic characteristics of the material must be accounted for to assess the feasibility of the novel technology.

In this thesis, the integrity of aluminum capping acting as an oxidation barrier has been thoroughly tested by exposing capped Permalloy samples to severe oxidizing environments. Additionally, changes in magnetic behavior due to oxidation and the chemical composition of the oxide forming on unprotected Permalloy have been investigated. Various sample treatments were utilized to force the oxidation process prior to magnetic characterization using vibrating sample magnetometry (VSM) and chemical analysis using X-ray photoelectron spectroscopy (XPS).

The protective capabilities of the Al capping layer were confirmed through the experimental work, indicated by the persistent magnetic moment of the samples having received the various treatments. On the other hand, the uncapped samples exhibited a significant loss of saturated magnetic moment equal to $\sim 8\%$ compared to the capped samples. Quantitative XPS analysis indicated that the predominant species forming on the unprotected Permalloy were antiferromagnetic NiO and ferrimagnetic $NiFe_2O_4$ and Fe_3O_4, in good agreement with the observed magnetic decay. Although a significant change in magnetic behavior was found for unprotected Permalloy, the implications on ASI structures are assumed to be of a minor character.

Sammendrag

Kunstige spinnis er metamaterialer bestående av nanoskala ferromagneter satt sammen i ulike geometrier for å produsere eksotiske magnetiske egenskaper og representerer potensielle kandidater for bruk i lavenergi ukonvensjonell databehandling. Utviklingen av denne teknologien avhenger i stor grad av å sikre en langsiktig stabilitet i de magnetiske egenskapene til nanomagnetene som utgjør spinnis systemene for å sikre ikke-flyktig informasjonslagring. I fabrikkasjon av kunstige spinnis systemer brukes som regel den magnetiske nikkel-jern legeringen $Ni_{80}Fe_{20}$ (Permalloy) sammen med et beskyttende aluminiumlag. Ettersom det er vel etablert at Permalloy danner oksidforbindelser som tilhører forskjellige magnetiske klasser er det nødvendig å redegjøre for effekten av disse på systemets totale magnetiske egenskaper for å vurdere fremtidsutsiktene til den nye teknologien.

I denne masteravhandlingen har aluminiums egenskaper til å beskytte magnetiske strukturer fra oksidasjon blitt utforsket ved å eksponere Permalloy-prøver beskyttet med aluminium til sterkt oksiderende miljøer. I tillegg har endringer i magnetisk oppførsel, som følge av oksidasjon, og den kjemiske sammensetningen av oksidlaget som dannes på ubeskyttet Permalloy blitt undersøkt. Ulike prøvebehandlinger ble tatt i bruk for å fremskynde oksidasjonsprosessen etterfulgt av magnetisk karakterisering gjennom vibrerende prøvemagnetometri og kjemisk analyse ved hjelp av røntgenfotoelektronspektroskopi.

De beskyttende egenskapene til aluminium ble bekreftet fra de eksperimentelle resultatene, indikert av vedvarende magnetisk moment for prøvene utsatt for ulike eksperimentelle behandlinger. I stor kontrast ble det funnet et betydelig tap av saturert magnetisk moment for de ubeskyttede prøvene, tilsvarende 8% sammenliknet med de beskyttede prøvene. Kjemisk analyse av oksidlaget dannet på de ubeskyttede prøvene indikerte at antiferromagnetisk NiO sammen med ferrimagnetisk $NiFe_2O_4$ og Fe_3O_4 dominerte sammensetningen til oksidet, i overenstemmelse med det observerte tapet av magnetisering. Selv om en betydelig endring i magnetisk oppførsel ble funnet for de ubeskyttede Permalloy-prøvene kan det med rimelighet antas at effekten av oksidasjon på kunstige spinnis systemer vil være av mindre betydning.

Preface

This Master's thesis concludes a five-year study program in nanotechnology with a specialization in nanoelectronics at the Norwegian University of Science and Technology (NTNU). The work presented was conducted over the spring semester of 2022, supervised by Professor Erik Folven and co-supervised by Dr. Jakob Vinje and Ph.D. candidate Anders Strømberg at the Department of Electronic Systems (IES) as partial fulfillment of the requirements for a degree of Master of Science in Nanotechnology.

I would like to thank my supervisors for their continued support and interest in my work throughout the semester. Their enthusiasm and competence in the field of magnetism is inspirational and have sparked many exciting discussions driving the work forwards. Last but not least, Erik, Jakob, and Anders are truly warm and friendly people, always having a witty comment at hand, making the Monday meetings enjoyable to the last end.

To my beloved family: your unconditional love and support means the world to me.

To all my friends in Timini and especially to my classmates: we have sung songs, we have stayed up late, we have laughed, and we have made the last five years truly memorable. For that, I am forever grateful.

Jonas Lyng-Jørgensen

Trondheim, June 2022

Contents

1 | Introduction

Background and motivation

In today's world, digital tools are increasingly becoming a necessity rather than just a privilege, and we are - now more than ever - relying on digital processing power and technological finesse to perform our everyday chores. A tremendous demand for data processing power has fueled the evolution of the key component in conventional computing: the *transistor*, responsible for the basic logic operations in our devices. Ever since the invention of the transistor, the performance of electronic devices has been improved by continuous miniaturization and denser packing of transistors on integrated circuits, as famously predicted by Gordon Moore in 1965 [1]. However, the success story of the transistor and the continued cramming of more devices onto integrated circuits is approaching its end, as state-of-the-art transistors are fabricated with a size close to that of a single atom [2]. On this length scale, and with a corresponding tight packing of the components, problems regarding leakage currents and heat dissipation start to tamper with the integrity of the devices, making the technology less feasible for sustaining the ongoing technological advances [3, 4].

As big data is getting bigger, the energy consumption related to information processing makes up an increasing fraction of our total energy budget. At the same time, the latest IPCC report commissioned by the UN declares code red for humanity, calling for sustainable solutions to combat climate change. The above represents huge incentives - ideological or pragmatic - to search for more energy-efficient digital technologies and has led researchers to look into the realm of *magnetic materials*. The ability of a ferromagnet to maintain its magnetization without any power supply can be regarded as a form of low-energy and *non-volatile* information storage, encoded in the direction of magnetization. Non-interacting nanomagnets are widely used for this purpose, where bits are encoded by forcing the magnetization of the magnets to assume one of two possible directions. By placing several nanomagnets in close proximity, effectively coupling them through their magnetic *stray fields*, the number of states for the coupled system increases exponentially with the number of coupled

nanomagnets [5].

What is described above has become known as *artificial spin ices* (ASI) and consist of interacting nanomagnets arranged at various geometries with the intention to produce "frustrated" magnetic moments. The frustration of the magnetic moments arises from the fact that the geometry of the ASI does not allow all the magnetic interactions of the array to be satisfied simultaneously, which may result in exotic magnetic behavior such as collective dynamics and highly degenerate energy states [6]. The complex collective dynamics exhibited by ASIs resemble the most sophisticated computer known to man - the human brain. This observation points toward the possibility to perform *in materio* calculations using the inherent physical phenomena of the ASI as computational primitives instead of logic operations, known as *neuromorphic computation.*

In neuromorphic computation, the topology of the brain is used as inspiration to form physical neurons interconnected by physical synapses with the ability to implement memory from the inherent physics of the materials [7]. An essential aspect of this emerging technology is to ensure non-volatile storage of information, and therefore, an integral part of the work is to understand the material system on which the technology is founded. By "industry standards" ASI systems are fabricated using the magnetic nickel-iron alloy Permalloy ($Ni_{80}Fe_{20}$) with a capping layer of aluminum to protect the magnetic structures from oxidation using a lithography process. However, fabrication via lithography and liftoff techniques leaves the sidewalls of nanomagnets exposed to the oxidizing atmosphere. Therefore, considering that iron and nickel form oxides belonging to various magnetic classes, the potential effects of oxidation on the magnetic characteristics of the material system need to be accounted for to ensure reliable information storage, making the novel technology feasible.

Objectives and outline

The objectives of this thesis are first to investigate the chemical composition of the oxide layer forming on unprotected Permalloy surfaces when exposed to extreme oxidizing environments and probe the potential consequences of oxidation on the magnetic characteristics of the material system. Secondly, the protective capabilities of aluminum capping layers acting as an oxidation barrier will be thoroughly tested to evaluate the current fabrication standard of ASI systems. Additionally, the magnetic anisotropy of Permalloy thin films will be explored to gain an improved understanding of the magnetic behavior of the Permalloy material system.

The stated objectives are pursued according to the following outline: chapter one presents relevant theory on magnetism and oxidation of metals, while the second chapter provides a theoretical background of the techniques used in the

experimental work. The third chapter explains the experimental procedure, including sample fabrication by means of photolithography, sample treatment, and characterization using x-ray photoelectron spectroscopy (XPS) to probe the chemical composition of the samples and vibrating sample magnetometry (VSM) to measure the macroscopic magnetization of the samples. The results and discussion section presents and discusses the results in the light of the presented theory and existing literature. Lastly, a conclusive remark is given, together with possible future work on the topic.

Note on units

Both the Système International d'Unites (SI) and the centimeter-gram-second (cgs) systems will be used throughout this work. The theory of magnetism will be presented in terms of SI units, while the results of the magnetic measurements will be given in terms of the electromagnetic unit (emu) belonging to the cgs system.

2 | Theory

This section will provide the reader with the necessary theoretical foundation to follow the experimental procedure and discussion of this work. The theory of magnetism and magnetic materials is based on *Magnetism and Magnetic Materials* by J.M.D. Coey, *Introduction to Solid State Physics* by C. Kittel and *Magnetism in Condensed Matter* by S. Blundell [8–10], while the theory on oxidation of metals is based on *Chemical principles* by S.S. Zumdahl [11]. Additionally, parts of the theory presented in this section are adapted from the work done in the specialization project TFE4570 over the fall semester of 2021 [12].

2.1   Classical magnetism

If you look closely, you will find that magnetism is, in fact, all around. The all-pervading magnetic field of the earth is, among many things, responsible for the magnificent color known as *aurora borealis*, lighting up the arctic winter sky. Traditionally, the magnetic field has also played an essential role in leading seamen to a safe haven with the help of a magnetic compass needle aligning with true north.

The striking resemblance of magnetic materials' attractive and repulsive forces to that of positively and negatively charged materials suggests that the two are somehow connected. This notion was captured by James Clerck Maxwell, who set out a unified theory of magnetism, electricity, and light, summed up in the four equations that bear his name:

$$\nabla \cdot \mathbf{B} = 0$$
$$\epsilon_0 \nabla \cdot \mathbf{E} = \rho$$
$$\frac{1}{\mu_0} \nabla \times \mathbf{B} = \mathbf{j} + \epsilon_0 \frac{\partial \mathbf{E}}{\partial t} \qquad (2.1)$$
$$\nabla \times \mathbf{E} = -\frac{\partial \mathbf{B}}{\partial t}$$

One of the consequences of the above equations that is emphasized in any introductory electromagnetics class is that the magnetic field, or the B-field, is free of divergence, $\nabla \cdot \mathbf{B} = 0$. Put differently, there can be no magnetic "sources" or "drains".

When describing magnetic materials, we introduce an auxiliary field, $\mathbf{H}$, where the auxiliary field and the magnetic field, $\mathbf{B}$, field are connected through the relation:

$$\mathbf{B} = \mu_0 \left(\mathbf{H} + \mathbf{M} \right), \tag{2.2}$$

where μ_0 is the magnetic permeability of vacuum and $\mathbf{M}$ is the macroscopic magnetization of a medium, which will be treated in depth in due time. In the literature, both the $\mathbf{B}$ and $\mathbf{H}$ fields are referred to as the magnetic field, therefore, for the sake of clarity, the auxiliary field $\mathbf{H}$ will be referred to as the magnetic field or *demagnetizing field* and the $\mathbf{B}$ will be referred to as the *magnetic flux density* throughout the thesis. Additionally, the magnetic field extending out of a magnetic material will be referred to as the magnetic *stray field*.

The compass needle aligning with the earth's magnetic field, with its magnetic north and south poles, can be modeled as a *magnetic dipole*. The north and south pole of the compass needle act analogous to a positive and a negative electric charge separated by a finite distance and carries a magnetic moment $\mathbf{m}$. The magnetic dipole moment, or simply dipole moment, is a useful abstraction when treating magnetism and represents the elementary magnetic quantity. From the classical approach to magnetism, following Ampere's law, the dipole moment is analogous to a current loop:

$$\mathbf{m} = I\mathcal{A} \tag{2.3}$$

where I is the circulating current through the loop and $\mathcal{A}$ is the area enclosed by the loop. The dipole moment points in the direction from the south pole towards the north pole.

When placed in an external static magnetic field the dipole moment has an associated energy called the *Zeeman energy*:

$$E_z = -\mu_0 \mathbf{m} \cdot \mathbf{H}. \tag{2.4}$$

From the equation, we observe that the Zeeman energy is minimized when the dipole moment and the external field are aligned, while the highest energy configuration is obtained when the dipole moment is oppositely aligned with the field.

2.1.1 Origin of magnetism

In a classical picture, magnetism is caused by moving electric charges. The counterpoint to this description is the quantum theory of magnetism which states

that macroscopic magnetism is caused by the quantized angular momentum of the elementary particles which constitute the material. Electrons and other nuclear particles carry an intrinsic angular momentum called *spin*, which gives rise to a magnetic moment. The spin magnetic moment, $\boldsymbol{\mu}_S$, is given by:

$$\boldsymbol{\mu}_S = \frac{e\hbar}{2m_e}\mathbf{S}, \tag{2.5}$$

where e is the electron charge, m_e is the electron mass and $\mathbf{S}$ is the spin angular momentum. The mass of the particles making up the nucleus of an atom is several orders of magnitude larger than the mass of an electron, and therefore we usually neglect the contribution from the nuclear particles to the spin magnetic moment. Consequently, we may regard the *atomic magnetic moment*, or simply magnetic moment, carried by an atom to be caused entirely by the magnetic moment of its electrons.

In addition to the intrinsic spin angular momentum of the electrons, the *orbital angular momentum* of the electrons, $\mathbf{L}$, related to the orbital motion of the electrons, contribute to an orbital moment. The orbital moment is the quantum analog to the circulating current producing a magnetic moment in the classical description of magnetism. Furthermore, the orbital angular momentum, $\mathbf{L}$ and the spin angular moment couples through *spin-orbit coupling* which makes up the total angular momentum $\mathbf{J}$ of the subatomic particles.

2.2   Magnetic materials

In the broader sense of the word, *magnetic materials* ususally refers to materials exhibiting a permanent magnetization such as the bar magnet found on refrigerator doors. The bar magnet is an example of a *ferromagnetic* material, which is one of several magnetic classes. *Magnetization* is a useful quantity when discussing different magnetic materials and is defined as the volumetric average of the atomic magnetic moments, $\mathbf{m}_i$:

$$\mathbf{M} = \frac{1}{V}\sum_i \mathbf{m}_i, \tag{2.6}$$

where V is the volume of the magnetic material and the summation is performed over all the atomic sites, i, of the material. From the above equation, we observe that the macroscopic magnetization of the material depends on the direction of the individual magnetic moments.
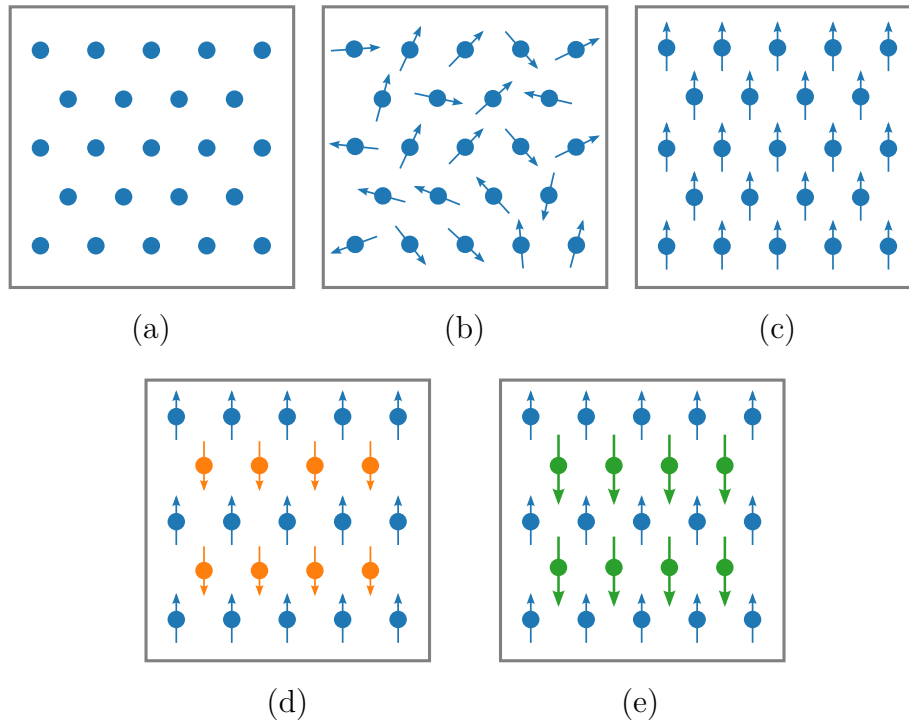
Figure 2.1: Schematic of the magnetic ordering in different magnetic classes. (a) Diamagnet with zero magnetic moments in the absence of an applied magnetic field. (b) Paramagnets with randomly oriented moments, resulting in a net zero magnetization. (c) Ferromagnet with spontanoeus magnetization due to exchange interactions. (d) Antiferromagnet with oppositely alligned moments, due to exchange interactions. (e) Ferrimagnet with nonzero magnetization due to oppositely alligned sublattices with moments unequal in magnitude.

Another important characteristic of magnetic materials is their response to an external magnetic field, that is, how the magnetization of the material changes when exposed to a magnetic field. This characteristic is called *magnetic susceptibility*, χ, and is defined as:

$$\chi \mathbf{H} = \mathbf{M}. \tag{2.7}$$

Magnetic materials such as *paramagnetic* and *diamagnetic* materials have linear relationships between the magnetization and external field, corresponding to a constant magnetic susceptibility, while *ferromagnetic* and *antiferromagnetic* materials exhibit non-trivial relations leading to more exotic behaviour such as *magnetic hysteresis*. In the following sub-sections some of the most common magnetic materials will be presented.

2.2.1 Diamagnetism

Diamagnetic materials are characterized by zero magnetic moments in the absence of an external magnetic field. However, when diamagnets are exposed to an external magnetic field, a small magnetic field is induced that opposes the direction of the applied field. The negative response of the diamagnetic materials can be explained by Faraday's law of induction which says that imposing a magnetic field will induce magnetic moments that oppose the applied field. Hence, the diamagnetic response is found in all materials, but the effect is relatively weak and is quickly dominated, for example, by the paramagnetic response.

2.2.2 Paramagnetism

Paramagnetic materials are characterized by randomly oriented magnetic moments in the absence of an external field and, therefore, a net-zero magnetization. When subjected to an external field, the individual atomic moments will minimize the Zeeman energy by aligning with the applied field, corresponding to a positive susceptibility. When removing the external field, the magnetic moments are randomized, yielding a net-zero magnetization of the material. The negative and positive susceptibility of diamagnetic and paramagnetic materials are shown schematically in figure 2.2, which illustrates that the paramagnetic response is also a weak effect, albeit more prominent than the diamagnetic response. The susceptibility of a paramagnetic material can be calculated using Langevin theory, in which we consider an ensemble of n randomized and noninteracting magnetic moments in an external field:

$$\chi = \frac{\mu_0 n m^2}{3 k_\mathrm{B} T},\tag{2.8}$$

where $m = |\mathbf{m}|$ is the magnitude of the magnetic moment, T is the temperature, and k_B is the Boltzmann constant. This is the classical form Curie's law:

$$\chi = \frac{C_\mathrm{Curie}}{T},\tag{2.9}$$

where $C_\mathrm{Curie} = \mu_0 n m^2 / 3 k_\mathrm{B}$ is the Curie constant.

2.2.3 Ferromagnetism

The characteristic feature of ferromagnetic (FM) materials is spontaneous magnetization due to the long-range ordering of the atomic moments in the material, which is caused by quantum mechanical *exchange interactions* between the electrons in the material. The quantum treatment of ferromagnetism is rather
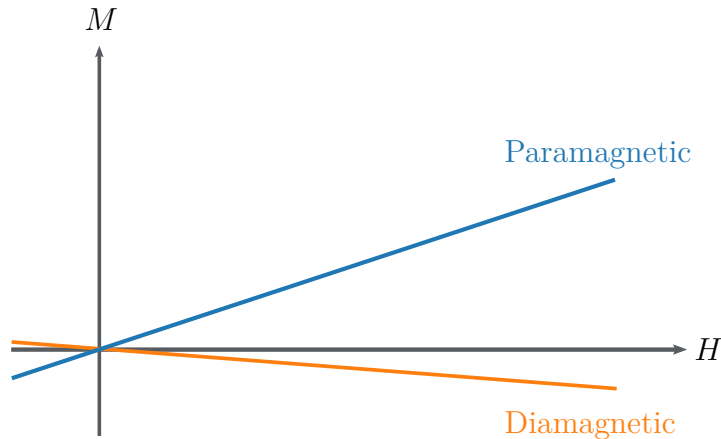
Figure 2.2: Schematic of the magnetic susceptibility for diamagnetic and paramagnetic materials. The small negative slope of the magnetic response for diamagnets indicates that the susceptibility is relatively weak.

tedious, and we may therefore opt for another theory of ferromagnetism that equally serves the purpose of this work, namely the molecular field theory proposed by Pierre Weiss in 1906. The initial idea of Weiss was that ferromagnets posessed an internal *molecular field*, proportional to the magnetization of the material. This molecular field, called *the Weiss field*, can thus be given as:

$$\mathbf{H}_{\mathrm{W}} = \gamma \mathbf{M}, \tag{2.10}$$

where γ is a proportinality constant. Combining the Weiss field with Langevin treatment of paramagnetism leads to Curie-Weiss law, which tells us that the ferromagnetic phase only exists below a critical temperature, T_{C}, called the *Curie temperature*:

$$\chi = \frac{C}{T - T_{\mathrm{C}}}. \tag{2.11}$$

Above the critical temperature $T > T_{\mathrm{C}}$, ferromagnetic materials behave as paramagnets.

Even though spontaneous magnetization exists in ferromagnetic materials, the summation of all the magnetic moments $\mathbf{m}_i$ of the material may also yield zero net magnetization. This fact can be ascribed to the formation of *magnetic domains*. A bulk ferromagnet lowers its free energy by forming magnetic domains, where the individual domains have coherent magnetization and are separated by *domain walls*. Therefore, net-zero magnetization can be obtained when the magnetic moments of the individual domains cancel out. The formation of magnetic domains is driven by the minimization of *magnetostatic energy*, which corresponds to minimizing the stray field extending outside of the material. When the magnetostatic energy dominates the energy landscape, ferromagnets will tend to form *flux-closure* configurations exhibiting virtually no stray field.
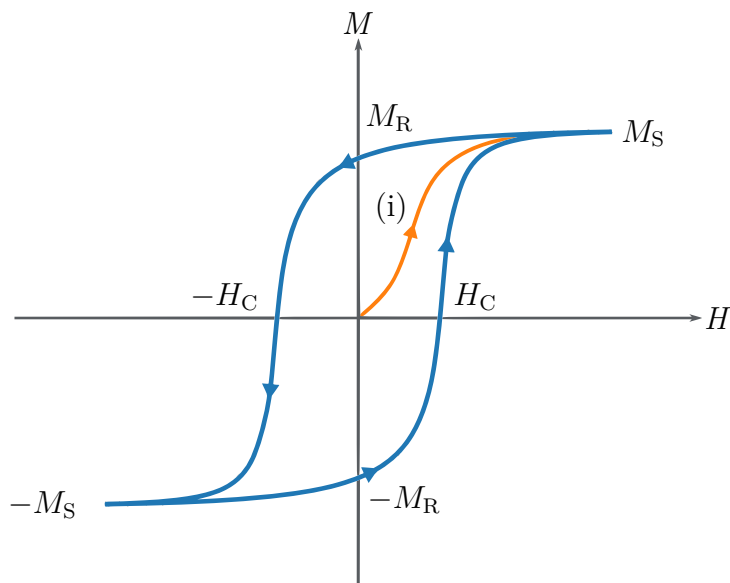
Figure 2.3: Plotting the magnetization of a ferromagnet versus the applied field yields the characterisitc magnetic hysteresis curve. Exposing a ferromagnet to a sufficiently strong magentic field, causes the magnetic moments of the material to allign with the external field, tracing out the virgin magnetization curve (i). For sufficiently strong fields the magnetization saturates, yielding a saturated magnetization M_S. Upon removal of the field after saturation, the ferromagnet remains magnetized with a remmanent magnetization M_R. The field strength required to switch the magnetization of the ferromagnet, H_C, is termed the coercive field.

The magnetic domains in ferromagnetic materials are also responsible for the magnetic hysteresis of ferromagnets, which is the curve obtained when plotting the magnetic moment of a ferromagnet versus an imposed magnetic field. Considering a ferromagnet with net-zero magnetization, the magnetization of the domains remains constant until an external field is applied, which causes the magnetization of the domains to start aligning with the imposed field. Plotting the magnetization of the ferromagnet versus the applied field as the ferromagnet evolves from a non-magnetized to a magnetized state traces out the *virgin magnetization curve*, indicated by the label (i) in figure 2.3.

Given a sufficiently strong field, the magnetization of all the domains will point along the applied field, resulting in a *saturated magnetization*, M_S. Upon removal of the external field, the ferromagnet remains magnetized with a remanent magnetization, M_r. The remanence is caused by *pinning* of the magnetic domains, which prevents the domains from evolving back to the initial non-magnetized state. In order to fully demagnetize the ferromagnet a characteristic field strength H_C, called the *coercive field*, is required. Ramping the external field until the ferromagnet reaches negative saturation and back to the positively saturated state traces out the characteristic magnetic *hysteresis*, shown schematically in
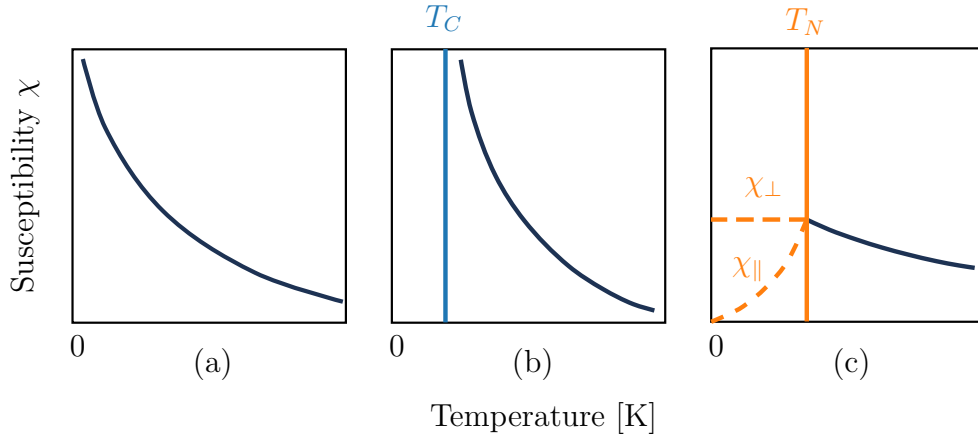
Figure 2.4: Schematic of the Curie-Weiss law describing the magnetic susceptibility as a function of temperature for (a) paramagnetic, (b) ferromagnetic, and (c) antiferromagnetic materials.

figure 2.3.

2.2.4 Antiferromagnetism

Antiferromagnetic (AF) materials represent another magnetic class which is, put it in the words of Lous Néel; "extremely interesting from the theoretical viewpoint but do not seem to have any applications".

In antiferromagnetic materials, the exchange interaction between adjacent atomic magnetic moments tends to align the moments antiparallel to each other, resulting in a net-zero magnetization. The antiferromagnetic ordering can be thought of as two oppositely aligned and interpenetrating sublattices of magnetic moments, as seen in figure 2.1 (d). The AF phase also only exists below a critical temperature, called the *Néel temperature*, T_N and the susceptibility can be fitted to the Curie-Weiss dependance with $\theta = -T_N < 0$:

$$\chi \propto \frac{1}{T - \theta} \quad \begin{cases} \theta = 0 & \text{Paramagnetic} \\ \theta > 0 & \text{Ferromagnetic} \\ \theta < 0 & \text{Antiferromagnetic.} \end{cases} \quad (2.12)$$

Schematic of the Curie-Weiss dependence of the magnetic susceptibility for paramagnetic, FM, and AF materials are shown in figure 2.4.

For an antiferromagnet, the net magnetization is zero unless the applied field is large [10]. Given a sufficiently strong magnetic field applied at a temperature below the Neel temperature, an AF can be magnetized in two possible ways, depending on the angle between the applied field and the direction of the two

sublattices. For a magnetic field applied perpendicular to the sublattices, the magnetic moments of both lattices will be canted towards the direction of the applied field, and for a sufficiently strong field, all moments will be aligned with the magnetic field. On the other hand, if a small magnetic field is applied parallel to the sublattices, the magnetic moments do not rotate but stay in line. Increasing the magnetic field to a critical field strength causes the system to snap into a different configuration through a *spin-flop* transition. The susceptibility for a field applied normal to and in parallel to the sublattices, $\chi_\perp, \chi_\parallel$, are shown schematically in figure 2.4.

Two examples of AF materials are NiO and FeO with Néel temeperatures of 525 K and 198 K respectively [13, 14]. The relatively high Néel temperature of NiO means that the compound appears with AF ordering in nature.

2.2.5 Ferrimagnetism

The last magnetic class which will be discussed is the class of *ferrimagnetic* materials, in which the atomic moments are arranged at two interpenetrating sublattices where the magnetic moments of the two sublattices differ in strength, resulting in a net magnetic moment. Ferrites are a family of ferrimagnetic materials with the chemical formula $MO \cdot Fe_2O_3$, where M is a divalent cation such as Fe_2^+ or Ni_2^+ [10]. Examples of ferrites are Fe_3O_4 and $NiFe_2O_4$. The susceptibility of ferrimagnets can have complicated temperature dependence and does not obey the Curie-Weiss law.

2.3 Magnetic anisotropy

Magnetic anisotropy refers to the tendency of the magnetization of a material to lie along preferred axes, called *easy axes*, while the less preferred axes are called *hard axes*. In the case of only one easy axis and one hard axis of magnetization, the system exhibits *uni-axial anisotropy*. The magnetic anisotropy may have several contributions, two of which are *magnetocrystalline anisotropy* and *shape anisotropy*. Magnetocrystalline anisotropy is an inherent, material-specific energy contribution reflected in easy and hard axes of magnetization along certain crystal directions. The magnetocrystalline anisotropy reflects the crystal symmetry and originates from the *crystal-field* and spin-orbit interactions in the solid or from interatomic dipole-dipole interactions.

Shape anisotropy is related to the geometry and arises when the symmetry of the sample is broken. For example, for a circular sample with perfect symmetry, there will be no preferred direction of magnetization given no other anisotropy contributions. On the other hand, a rectangular sample with reduced symmetry will favor magnetization along its long axis. This effect is a direct consequence
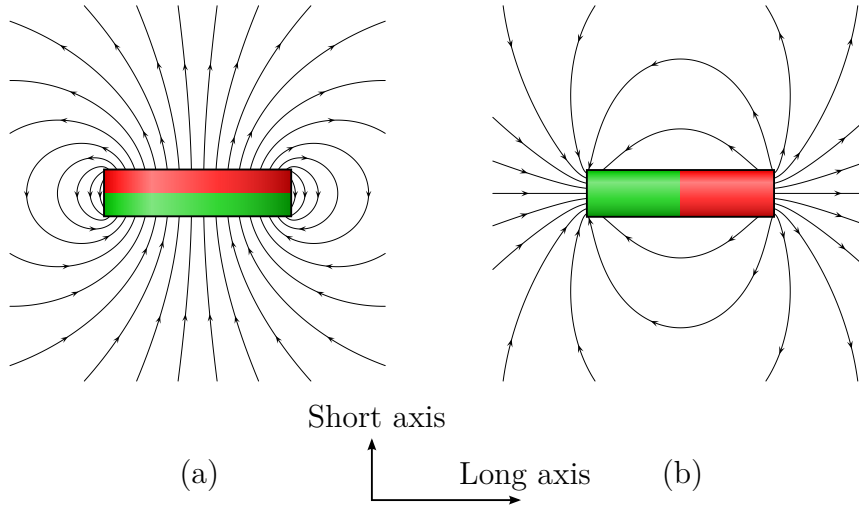
Figure 2.5: Stray field produced by a bar magnet that is magnetized along its (a) short and (b) long axis. The energy stored in the stray field is reduced by assuming a magnetization along the long axis of the magnet, giving rise to magnetic shape anisotropy.

of the minimization of the *magnetostatic energy* stored in the stray field. The minimization of the stray field can be visualized in figure 2.5, where a rectangular sample magnetized along its long axis produces a significantly smaller stray field than a sample magnetized along its short axis. In the case of a *unidirectional anisotropy*, where there is one preferred direction of magnetization, we call the preferred direction the *easy axis* and the direction normal to the preferred axis the *hard axis* of magnetization. The easy and hard axes of magnetization are clearly reflected in magnetic measurements due to qualitatively different magnetization dynamics for the two directions.

In the case of the nickel-iron alloy $Ni_{80}Fe_{20}$, the magnetocrystalline anisotropy is close to zero and quickly dominated by shape anisotropy if the symmetry of the sample is broken [15]. In the case of magnetic thin films, the main subject of this work, the shape anisotropy of the film favors magnetization in the film plane.

2.3.1 Exchange anisotropy

When placing a ferromagnetic and antiferromagnetic material in contact, the magnetic moments of the materials may couple at the interface, resulting in an *exhcange-bias* or *exchange anisotropy*. Exchange biasing of a ferromagnetic material by coupling with an AF layer causes a unidirectional exchange field, competing with the applied magnetic field [10]. If the exchange field points in the same direction as the applied field, the exchange coupling can be observed by measuring a shifted hysteresis loop. If the two fields are at right angles, a

hard axis response is obtained, corresponding to a lower coercive field and a qualitatively different shape of the measured hysteresis [10].

2.4 Oxidation of metals

The chemical reaction in which a metal, M, reacts with oxygen, O_2, to form a metal oxide can be described by the relatively simple equation:

$$x\mathrm{M} + \frac{y}{2}\mathrm{O}_2 \rightleftharpoons \mathrm{M}_x\mathrm{O}_y, \qquad (2.13)$$
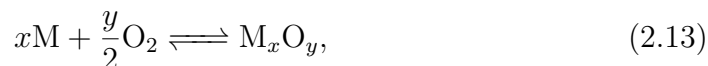
where the driving force of the oxidation reaction is the free energy change associated with the formation of the oxide from the reactants. However, one should not be fooled by the above equation, as the formation of oxides from a pure metal is far from trivial. As K. R. Lawless puts it: "Although the overall chemical reaction seems very simple, the progress of the reaction is in most cases determined by phase boundary reactions and diffusion processes which can be, and usually are, very complex" [16]. Due to the complex nature of the oxidation processes, only a short review on the topic will be provided in this section, while a more thorough treatment can be found in the previously cited work of K.R. Lawless: *The oxidation of metals.*

2.4.1 Chemical equilibrium and kinetics

If energetically favorable, a chemical reaction will proceed until the concentration of the reactants and products stays constant over time, which is termed *chemical equilibrium.* Qualitatively the dynamics of chemical equilibrium can be understood in terms of *Le Châtelier's principle* which says that: "if a change in conditions is imposed on a system at equilibrium, the equilibrium position will shift in a direction that tends to reduce that change in conditions" [11]. For example, increasing the pressure by adding a reactant will cause the system to compensate for the imposed change by shifting the equilibrium towards the products of the chemical reaction. Thus, considering the dynamical equilibrium of the oxidation reaction described in equation 2.13, an increased the partial pressure of oxygen will cause the equilibrium to shift towards the metal oxide, translating to a higher degree of oxidation.

Chemical equilibrium considerations can provide information about the shift towards reactants versus products for a chemical reaction. However, we are often also interested in the rate at which the reaction proceeds, governed by *chemical kinetics* and described mathematically by the chemical *rate constant, k*. The effect of elevated temperatures and increased partial pressure of reactants on the rate constant can be understood by considering the *collision model*. This model is based on the assumption that reactants need to collide and have an

energy equal to, or greater than, the *activation energy* of the reaction for the colliding reactants to form the product. Taking these factors into account, the rate constant can be given by:

$$k = zpe^{-E_a/RT} \tag{2.14}$$

where E_a is the activation energy of the reaction, R is the gas constant, T is the absolute temperature of the system, z is the collision frequency and p is the steric factor which reflects the fraction of collisions with effective orientations of the colliding reactants. Rewriting the above equation by substituting the two latter constants by a frequnecy factor $A = zp$, we obtain *Arrhenius equation* describing the rate constant:

$$k = Ae^{-E_a/RT}. \tag{2.15}$$

In the Arrhenius equation, the exponential represents the fraction of collisions with sufficient energy to produce the chemical reaction. The equation clearly shows that the reaction rate increases exponentially with temperature, $k \propto e^T$. Using the ideal gas law, $PV = nRT$, it can also be shown that the collision frequency is proportional to the partial pressure of the reactant, $z \propto P$. Thus, increasing the temperature and the partial pressure of the reactants function as an effective means of speeding up a chemical reaction.

3 | Fabrication and Characterization Techniques

This chapter aims to provide a theoretical foundation for the fabrication and characterization techniques used in the experimental work. In the experimental work, photolithography was utilized to fabricate the various samples, which subsequently were characterized using vibrating sample magnetometry (VSM) and x-ray photoelectron spectroscopy (XPS). The theory on photolithography is mainly based on the work from the specialization project performed in the fall of 2021, while the theory on XPS and VSM is based on *Photoelectron spectroscopy: principles and applications* by S. Hüfner, and *The vibrating sample magnetometer: Experiences of a volunteer* by S. Foner [12, 17, 18].

3.1 Photolithography

Photolithography is a microfabrication technique that is used to fabricate structures on the micro-and nano-scale. In photolithography, an ultraviolet light source is used to transfer a latent image onto a light-sensitive polymer substance called a *photoresist*. Using a positive(negative) photoresist, the areas that are exposed to the UV light are made more(less) soluble when exposed to a *developer*, which is used to develop the latent image. The developed resist structure may be used in further processing steps, which typically include metal deposition. After depositing the metal, the resist structure can be stripped off in a lift-off process, leaving a patterned metal structure. The photolithography process is well established and involves a multitude of steps depending on the desired outcome. However, the basic process steps may be summed up as a) substrate priming, b) spin coating, c) exposure, d) development, e) metallization, and f) lift-off, shown schematically in figure 3.1.
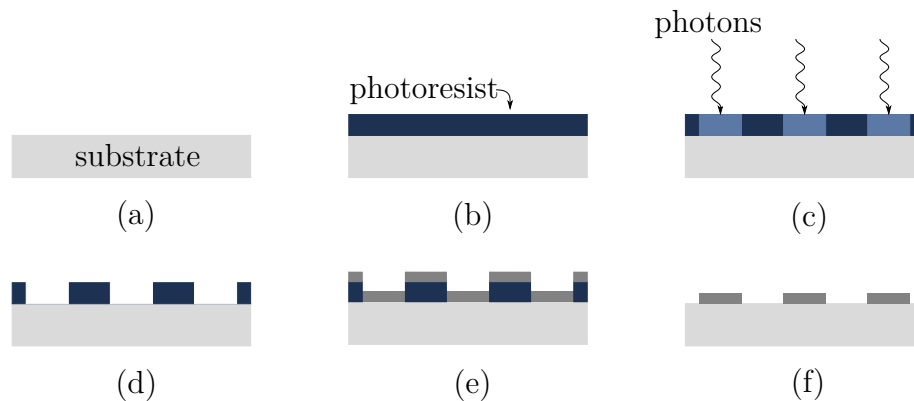
Figure 3.1: Schematic illustration of the photolithography process. (a) The substrate on which the resulting structure is made, usually a Si wafer, is a planar surface that should have good adhesion to the photoresist. (b) A photoresist is spin-coated onto the substrate with fitting parameters to create a thin resist layer. (c) The resist layer is exposed with photons, making the exposed areas more soluble in contact with a developer when using a positive resist. (d) The exposed areas of the resist layer are removed using a developer. (e) A metal layer is deposited on top of the resist structure. (f) The remaining resist and the metal on top of the resist are removed in a lift-off process.

3.2 X-ray photoelectron spectroscopy

X-ray photoelectron spectroscopy (XPS) is a surface analysis technique that allows for determining the chemical composition of a sample surface. The technique is based on the use of high-energy x-ray photons with sufficient energy to dislodge electrons from the target material through a process termed the *photoelectric effect*, which was famously described by Einstein in his paper on the creation and transformation of light in 1905 [19]. The liberation of a so-called *photoelectron* leaves behind a *photoionized* atom with a positive charge due to the removal of a negative electron. After the liberation of the photoelectron, the electrons bound to the photoionized atom will rearrange to lower the energy of the atom through processes that can be quite complex due to electron-electron interactions in the solid. Therefore, the final state of the atom may be substantially different from the initial state.

Due to energy conservation, the kinetic energy of the photoelectron will reflect the energy difference between the final and initial state of the atom from which it originated. By identifying that electrons reside in well-defined energy levels characteristic of different chemical compounds, the detection of electrons according to their kinetic energy allows identifying the chemical compound from which it originated. In a very simplified picture, this is the working principle of the XPS technique as the detected electrons that are allowed to escape the material without losing their energy will make up a well-defined signal, corresponding to a characteristic energy transition in the "parent compound".

The measured signal of the electrons residing in the core energy levels of an atom will take the form of a *Lorentzian* lineshape, where the full width at half maximum (FWHM) is a convolution of the instrumental linewidth and the lifetime broadening of the *core hole*. In theory, the energy of the core electron is well-defined and should assume the form of a delta function; however, the finite time it takes for an electron to relax into the core hole causes an uncertainty in the measured electron energy, which broadens the measured signal.

Acquisition of XPS spectra

In order for the photoelectric effect to take place, the energy of the photon impinging on the target material must exceed the characteristic *work function*, ϕ, of the material, corresponding to the energy required for an electron to escape the material. The kinetic energy of the electrons, E_{kin}, can then be given as:

$$E_{\mathrm{kin}} = \hbar\omega - \phi, \tag{3.1}$$

As discussed above, the energy of the electrons that are allowed to escape the material without losing their energy to inelastic scattering events will reflect the *binding energies*, E_{B}, of the material. Therefore the energy of the electrons may also be given in terms of the binding energy:

$$E_{\mathrm{kin}} = \hbar\omega - \phi - E_{\mathrm{B}}. \tag{3.2}$$

For a solid material the binding energy is referenced to the *Fermi energy*, $E_{\mathrm{B}} = 0$ at E_{F}.

An electron analyzer can detect photoelectrons according to their kinetic energy as discrete events. One example of an electron analyzer is the *spherical deflection analyzer* (SDA), or hemispherical analyzer, consisting of two concentric hemispheres with an applied voltage over the hemispheres. The potential gradient between the two hemispheres sets up an electric field that affects the path of the electrons that enter the analyzer and allows only electrons with specific kinetic energy to exit the analyzer. The specific energy required to pass through the analyzer and reach the detector is termed the *pass energy*, E_{pass}. One operating mode of the hemispherical analyzer is the constant pass energy mode, or fixed analyzer transmission (FAT). In this operating mode, the potential over the hemispheres is kept constant while the magnetic lenses of the XPS system scan over different electron energies. The relationship between the pass energy and the voltage drop over the hemispheres can be given by:

$$E_{\mathrm{pass}} = eV \left(\frac{R_{\mathrm{o}}}{R_{\mathrm{i}}} - \frac{R_{\mathrm{i}}}{R_{\mathrm{o}}} \right)^{-1} \tag{3.3}$$

where e is the electron charge, V is the voltage drop over the two hemispheres, R_{i} is the radius of the inner and R_{o} is the radius of the outer hemisphere, as
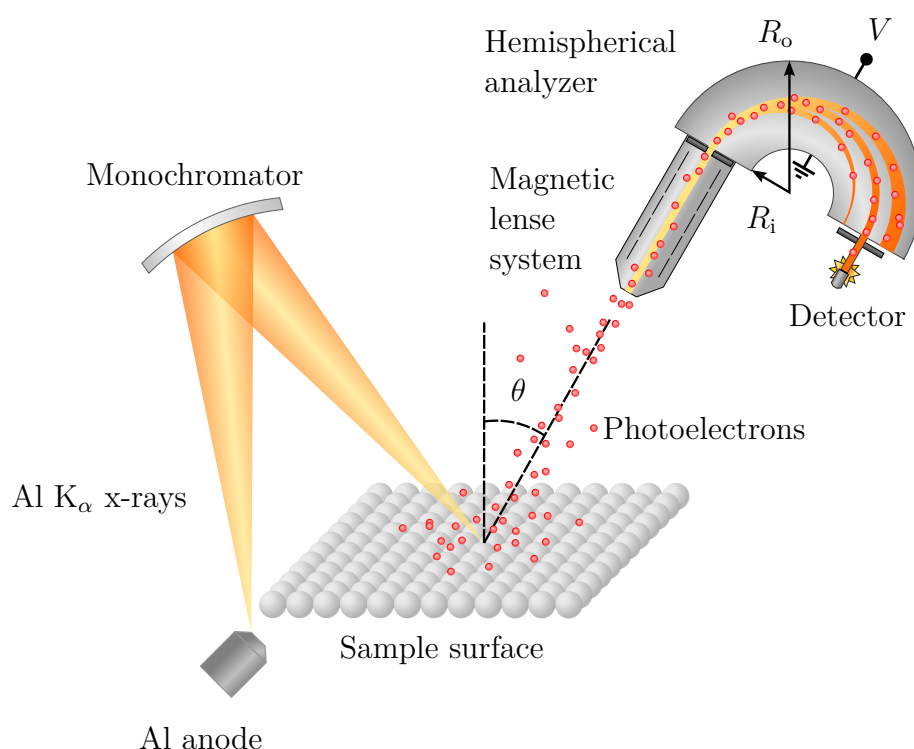
Figure 3.2: Schematic of an XPS measurement setup using the Al K$_\alpha$ x-ray line. A monochromator filters the x-rays produced from the Al anode before imping on the target sample. Photoelectrons that are liberated from the sample enter the magnetic lens system and the hemispherical analyzer, and are counted at the detector as discrete events.

indicated in figure 3.2 [20]. Even though the electrons are detected and counted according to their kinetic energy, we normally use the binding energy as abscissa when displaying the electron count of an XPS measurement.

Features of XPS spectra

Electrons are detected as discrete events, and the number of detected electrons for a given detection time and energy is displayed. A typical XPS spectrum contains several well-defined peaks caused by elastically scattered electrons together with a background signal caused by electrons that have suffered energy loss due to inelastic scattering. Due to the fact that electrons are removed from the sample, charge buildup can arise on the sample surface, which causes a shift in the measured peaks. This shift can be adjusted in the processing of the experimental data. The different features of XPS spectra originate either from the physical and chemical nature of the sample, fundamental features of the XPS technique, or instrumental effects. In what follows, a brief description of various *lines* appearing in XPS spectra is given.
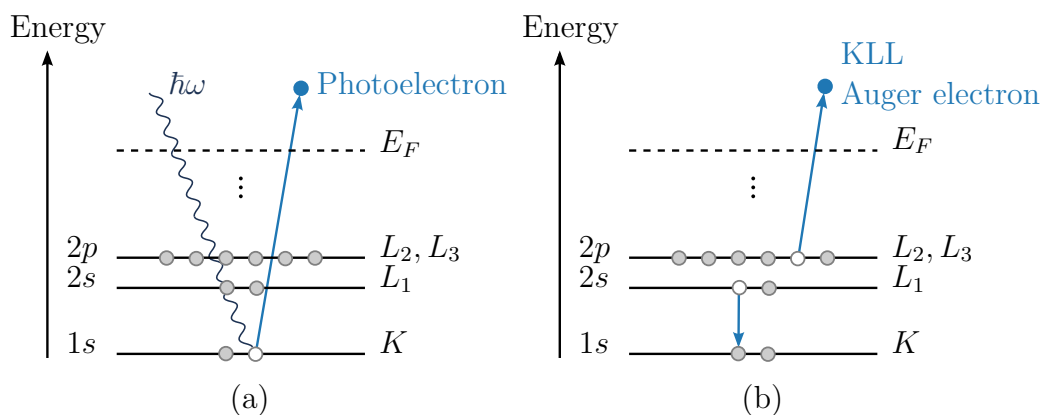
Figure 3.3: Energy level diagram with schematic visualization of the (a) direct photoemission and (b) auger electron emission processes.

Direct photoemission lines

The direct photoemission lines are caused by photoionization, where a photon transfers its energy and dislodges an electron from the solid sample. This process causes the most intense and symmetric peaks of an XPS spectrum and is shown schematically in figure 3.3 (a).

Auger lines

Another prominent feature in XPS spectra is *Auger lines* resulting from the emission of Auger electrons. This process initially proceeds as the direct photoemission process, which leaves behind a core hole. When an electron relaxes from a higher energy state to the core hole, energy is conserved either via the emission of a photon or an electron with energy equal to the energy difference between the core level and the initial energy of the electron relaxing into the core hole. In the case of an electron being liberated upon relaxation, we obtain what is called an *Auger electron*, visualized in figure 3.3 (b). The Auger lines of XPS spectra are named by specifying the initial and final vacancies in the Auger transition. For example, the LMM lines are caused by an electron from energy level M relaxing to L, causing an Auger emission from the M level. Here, L and M are the x-ray physics notation for the energy states indicated by the quantum numbers $n = 2$ and $n = 3$ respectively. A complete list of the quantum numbers and the corresponding spectroscopic and x-ray physics notations is given in appendix D.
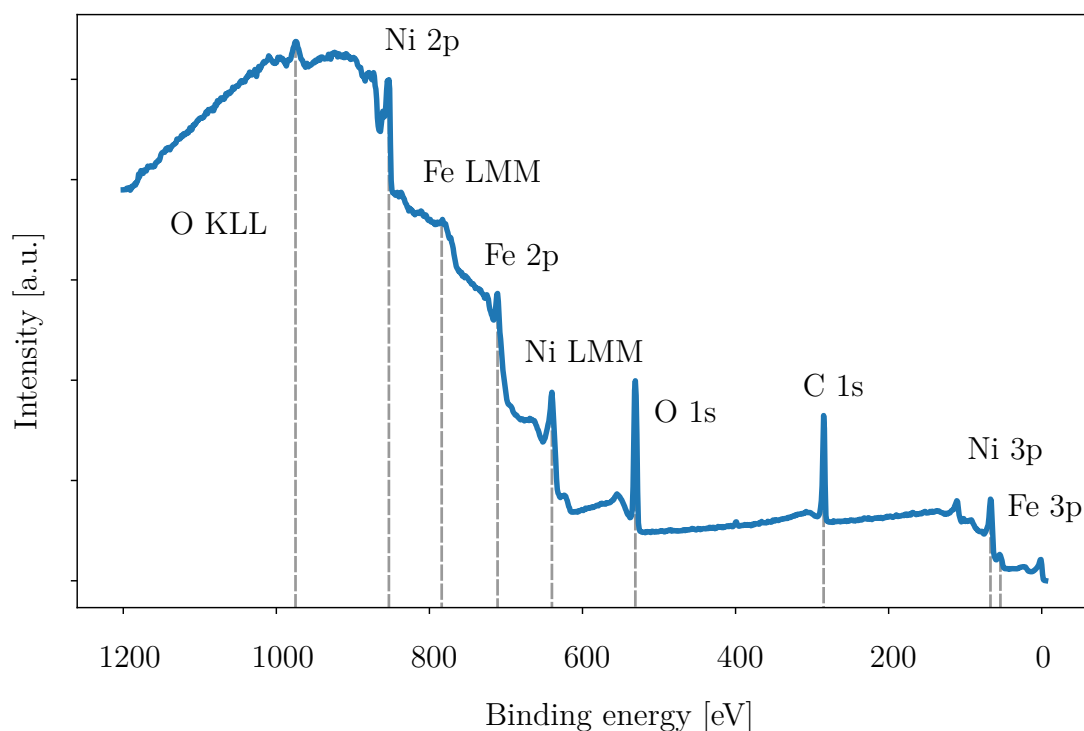
Figure 3.4: Example of an XPS wide scan showing various labelled peak features. The most prominent peak features are caused by direct photoemission of various chemical species.

X-ray satellite lines

The "monochromatic" Al K_α x-ray source used in the XPS measurements is, in fact, not entirely monochromatic and exhibits other characteristic x-ray components at higher photon energies. Therefore, for each photoelectron peak resulting from the main x-ray component of the Al K_α source, there are additional minor peaks called *satellites*, having an intensity and energy spacing characteristic of the x-ray anode material.

Multiplet splitting

When a core electron is dislodged from an atom that has unpaired valence electrons, the photoelectron can create a vacancy in the core level in several possible ways due to the spin-orbit coupling between unpaired electrons in degenerate orbitals. The spin-orbit coupling causes degenerate energy levels to split into multiple energy levels corresponding to $j = l \pm 1/2$, where the energy splitting is due to parallel and anti-parallel alignment of the orbital magnetic moment and the spin magnetic moment. For example, for the 2p-shell, the

spin-orbit coupling causes the degenerate 2p energy level to split into a $2p_{1/2}$, $2p_{3/2}$ doublet. The doublet lines may be resolved in an XPS measurement and are often evident in the first-row transition metals such as Ni and Fe [21].

Chemical shifts

When probing the surface of a sample with the XPS method, we are usually not interested in the binding energy of a particular core level but rather the change in binding energy between two chemically different forms of the same atom. This energy shift is called a *chemical shift*. This effect can be described in a simplified representation by considering metals and their oxide compounds. Metal in its oxidized state attains a positive charge, M^+, which translates to a lower screening of the nucleus potential, resulting in higher binding energy for the core electrons. Therefore, the metal oxide compounds of metals appear to shift to higher binding energies with respect to the main metallic peaks in XPS spectra.

Sampling depth

The Al K_α x-ray line used in this work consists of highly energetic photons with an energy of 1486.6 eV [21], which allows the photons to penetrate, and possibly transmit through, solid matter [22]. However, the limiting factor of the XPS technique's probing depth is not the penetration depth of the x-rays but rather the distance over which the photoelectrons can travel without losing energy via inelastic scattering events. This distance is called the *inelastic mean free path* (IMFP), λ_e. The *sampling depth* can be defined as the thickness over which 95% of the detected photoelectrons are generated, given by:

$$t \equiv 3\lambda_e \cos\theta_e, \tag{3.4}$$

where θ is the angle of photoelectron emission with respect to the sample surface normal, as indicated in figure 3.2. The sampling depth of the XPS technique is usually on the order of a few nm [21].

Background and peak models

When analyzing XPS spectra, the well-defined photoemission lines sit on top of a background signal. The background signal contains valuable information about the system; however, the zero energy-loss signal must be separated from the inelastically scattered background to perform a quantitative analysis of the XPS spectra [23]. Hence, background subtraction is an integral part of the analysis of experimental XPS data. Two widely used background models are the Shirley background, and the Tougaard background [24], and the former of the two will be used exclusively in this work.

After background subtraction, the experimental data can be curve-fitted by forming a *peak model* comprised of *peak components*. The peak components of the model are specified with a *lineshape*, which is a mathematical function, together with fitting parameters. In this work, the peak components are modeled using *Voigt* lineshapes which are formed by convoluting a gaussian and lorentzian lineshape. Usually, several peak components are fitted to the spectrum, which in sum makes up an *envelope function*, fitting the experimental data. In theory, one may include an infinite number of component peaks to fit the experimental data perfectly. Therefore, tabulated values for peak binding energies and FWHM for chemical compounds should be used to produce a physical model. In the end, fitting a peak model to experimental XPS data is highly prone to human error and may result in unphysical models. Therefore, an essential part of the curve fitting is the assessment of the "goodness of fit" for the different peak models.

Evaluating goodness of fit

Several figures of merit can be used to assess the goodness of fit of a peak model. The *chi-squared* parameter indicates the standard deviation of the residual between the envelope function and the experimental data. The *reduced chi-squared* parameter can be used to account for the number of peak components in the peak model and is given by the chi-squared divided by the number of free parameters used in the curve fit. Additionally, the *Abbe criterion* indicates how the residuals of a peak model are distributed. The abbe criterion is especially useful in determining if a peak model is consistently below or above the experimental data and will be used together with the reduced chi-squared parameter to assess the peak models in the experimental work.

3.3   Vibrating sample magnetometry

Vibrating sample magnetometry (VSM) is a class of magnetic measurements where the macroscopic magnetization of a sample is measured. The technique was first developed by Foner in the 1950s and is based on driving a magnetic sample with an oscillatory motion while subject to a uniform magnetic field [25]. According to Faraday's law of induction, an oscillating magnetic sample will induce an electromotive force that can be detected by a conducting coil. The linear motor drives the sample, attached to a sample holder, at a frequency, f, with a fixed amplitude A. The electromotive force, $\mathcal{E}$, can then be calculated from:

$$\mathcal{E} = mGA \cdot \omega \cdot \cos(\omega t), \tag{3.5}$$

where $\omega = 2\pi f$ is the angular frequency, m is the magnetic moment of the sample, G is a geometry factor of the detection coil and t is the time [18].

In this work, a Quantum Design Versalab system with a VSM module is used, and a schematic of the system is shown in figure 3.5. The electromagnet of the VSM is mounted such that the applied magnetic field is parallel to the detected magnetization. Other detection coil geometries allow measurement of the magnetization both parallel and normal to the applied magnetic field. Due to the detection coil geometry of the Versalab system, the sample has to be rotated physically to be able to investigate the magnetic anisotropy of the sample.
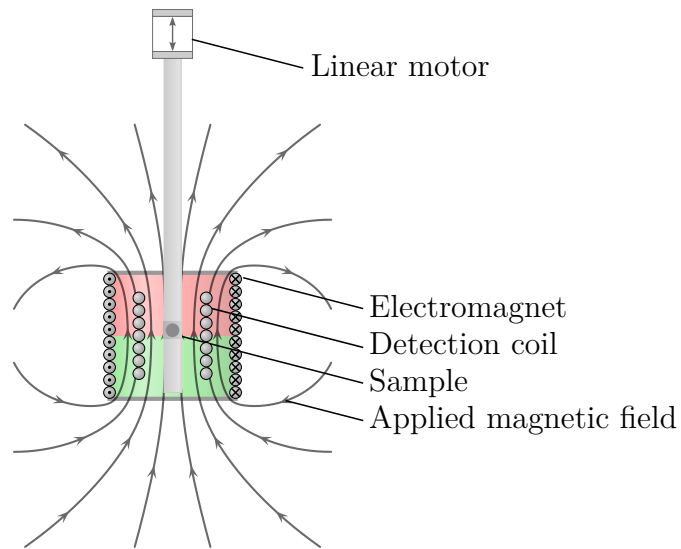
Figure 3.5: Schematic of the VSM module used in the experimental work.

4 | Experimental

The experimental work of this thesis can be divided into three parts: sample fabrication, sample treatment, and, lastly, sample characterization. This chapter describes the sample fabrication using a lithography process to fabricate Permalloy samples with and without a protective Al capping layer. Subsequently, an account is given of the various sample treatments used to force and speed up the oxidation reaction to various extent. The parameters used in XPS and VSM measurements are then given together with a review of the data processing performed on the raw experimental data. Lastly, the work performed to investigate magnetic anisotropy in Permalloy thin films is described, with an emphasis on TEM image processing.

Scribe

$l = 4$ mm
$r = 1.75$ mm
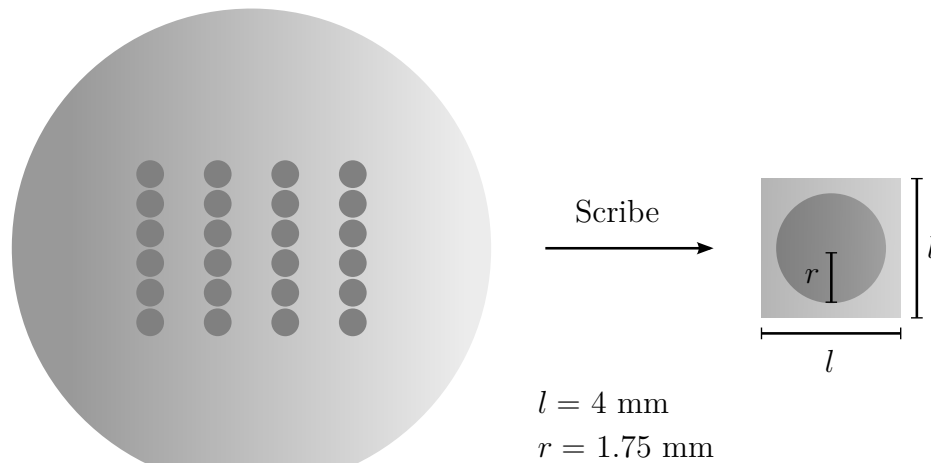
Figure 4.1: Schematic of the metalized two-inch wafer used in sample fabrication and the scribed samples used in VSM and XPS measurements. The dimensions of the final samples are indicated in the figure.

4.1   Sample fabrication

The samples used to investigate the effect of oxidation on Permalloy and Aluminum surfaces were given the geometry of circular thin films with a radius of 1.75 mm, where the relatively large radius of the disks was chosen to fit the sample holder of the VSM and, at the same time, ensure a sufficiently strong VSM signal. Complying with fabrication standards of ASI fabrication, a 20 nm thick layer of Permalloy was used as a default thickness for the fabricated samples. Samples intended for investigating the integrity of Al as a protective capping layer were prepared by depositing an additional 2.5 nm Al layer on top of the Py thin film. On the contrary, the Al layer was omitted for samples intended for chemical analysis of the oxide layer. For clarity, the samples fabricated with a protective Al layer will be referred to as *capped samples* while the pure unprotected Permalloy samples will be referred to as *uncapped samples* throughout the thesis.

Additionally, samples with different metal thicknesses were fabricated to enable interpolation of the saturated magnetic moment of the thin films as a function of the film thickness. Having settled for 20 nm as the default metal thickness, it was opted to fabricate samples with Permalloy thicknesses of 10 nm and 40 nm to obtain data points for thinner and thicker magnetic films. Additionally, several batches of capped and uncapped samples were fabricated due to an observed magnetic anisotropy in the initial fabricated batches. A complete list of the different fabricated samples and their experimental purpose is given in appendix A.

Photolithography was performed at the NTNU NanoLab cleanroom facilities using a maskless aligner, MLA150, together with the positive photoresist SPR700. The mask design used consisted of 24 disks evenly spaced over a two-inch Si [100] wafer, shown schematically in figure 4.1. After the development of the photolithography structures, metallization was performed using a Pfeiffer E-Beam evaporator, depositing both Permalloy and aluminum at a rate of ∼1 Å/s by manual operation of the instrument. While evaporating the metal onto the samples, the substrate was rotated inside the vacuum chamber to produce a homogenous metal layer. Finally, liftoff was performed on the metalized samples by immersing the samples in acetone and utilizing an ultrasonic bath for approximately two minutes. The finished metal disk samples were then scribed into pieces of 4 mm×4 mm using a manual wafer scriber to fit the sample holder of the VSM. All the steps performed and a detailed description of the parameters used in the lithography process are given in table 4.1.

Table 4.1: Photolithography steps performed in the sample fabrication.

Process step	Description
Wafer priming	Rinse in acetone followed by IPA. Blow dry with nitrogen. Plasma cleaning, 10 minutes at 600 sccm O_2 and 1000 W.
Dehydration bake	5 min at 150 °C.
Spin coating	SPR700 photoresist spin coated for 34 seconds at 4000rpm using an acceleration of 1000rpm/s.
Soft bake	1 minute at 95°C.
Exposure	Exposure performed using an MLA150 with a dose of 120 mJ/cm².
Develop	Ma-D 332:DI water at a 2:1 ratio followed by rinse in DI water. Blow dry with nitrogen.
Metallization	Metallization of Py/Al with a rate of ~ 1 Å/s
Lift-off	Lif-off performed in an ultrasonic bath for 2 minutes using acetone. Rinse in IPA and blow-dry with nitrogen.

4.2 Forced oxidation of capped and uncapped samples

To produce an appreciable difference in the degree of oxidation between the treated and the control samples, it was opted to expose the samples to the most severe oxidizing environments found at the NanoLab facilities: oxygen plasma and hot baking. As a reference to the treated samples, an experimental group was left subjected only to the ambient atmosphere of the lab facilities prior to XPS and VSM measurements. The samples treated with oxygen plasma were treated for 30 minutes at 600 sccm O_2 and 1000 W. Samples treated with a hotplate were baked at 150 C° on top of a carriage wafer for approximately 60 minutes. Due to heat loss through the carrier wafer and the sample itself, the temperature on the sample's surface was measured to be approximately 105 C° using a laser thermometer. The increased partial pressure of oxygen obtained in the plasma cleaner and the elevated temperatures in both the plasma cleaner and at the hotplate were chosen to produce a substantial difference in the chemical rate constant with respect to the control samples.

The sample treatment was performed on capped and uncapped samples to produce different outcomes. First, the capped samples were treated to assess the resilience to extreme oxidizing environments and thus evaluate the integrity

of the material as a protective oxidation barrier. On the other hand, the treatment was performed for the uncapped samples to assess the potential loss of magnetic moment due to oxide formation and to probe the chemical composition of the oxide layer for different degrees of oxidation. Both the sample fabrication and the subsequent sample treatment were performed a few days prior to XPS measurement to limit the time of exposure to the ambient oxidizing atmosphere. The samples belonging to the different experimental groups (plasma-treated, hotplate treated and control samples) will be referred to according to their respective treatments throughout: namely as *plasma*, *hotplate* and *control* samples.

4.3 XPS measurements

The XPS measurements were performed on the variously treated samples at NTNU using a Kratos AXIS Ultra instrument with an Al K$_\alpha$ x-ray source. In addition to the uncapped control, hotplate, and plasma samples, an uncapped control sample from the first fabricated batch was included to assess the over time effects of exposure to the ambient atmosphere. Before measurements, the samples were mounted on a sample holder and installed in the XPS. After obtaining a satisfactory vacuum in the measurement chamber, the measurement signal was optimized by scanning the O 1s spectrum and adjusting the x-ray beam to obtain a strong measurement signal.
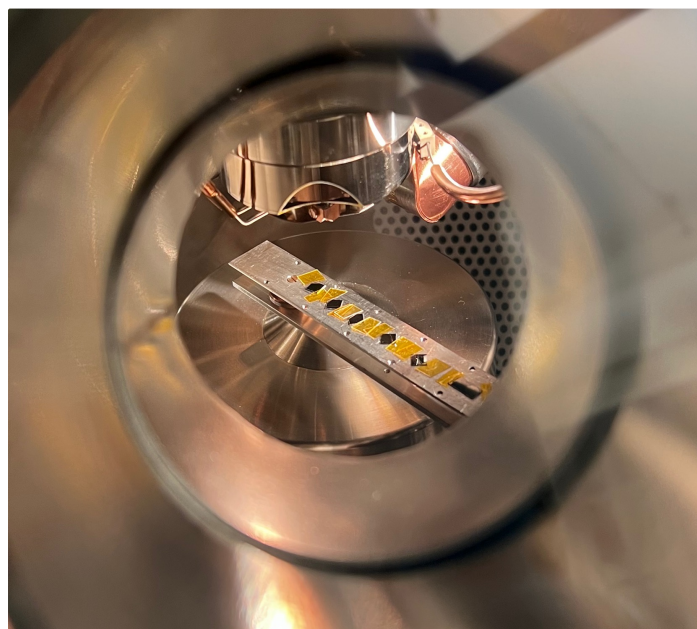

Figure 4.2: Image of the capped samples installed in the XPS measurement chamber.

The measurement series performed on each sample consisted of an initial wide scan sweeping electron energies from 1200 - 0 eV, followed by several detailed scans of interest, including the C 1s, O 1s, Si 2p, Al 2p, Ni 2p, Fe 2p, and Fe 3p spectra. The first XPS measurement was performed on the uncapped samples, for which it was opted to scan for iron in the Fe 3p energy range inspired by similar works performed in the literature. In order to reduce the amount of noise in the measurements, all scans were performed twice and averaged. A list of measurement parameters used in the individual scans is given in appendix B.

XPS data processing

The experimental XPS data was processed using CasaXPS, a spectral processing and interpretation framework widely used in the interpretation of XPS spectra [26]. The first processing step performed on the raw data was to correct for charge buildup during measurements by localizing the main C 1s peak caused by adventitious carbon on the sample surface and subsequently shifting all spectra performed on the individual samples by the measured offset from the true C 1s peak binding at 284.8 eV [21]. The second step of the processing was to fit an appropriate background to the raw data. The Shirley background was used for all the obtained spectra by manually setting a region that limited the part of the spectrum of interest. For example, for the Ni 2p spectrum, only the Ni $2p_{3/2}$ part of the spectrum was relevant for the data analysis, and therefore limits were set to include the peak features in this region.

Curve fitting of the experimental data was performed by consulting literature, in which similar measurements had been performed, with tabulated peak binding energies for different chemical species and their respective FWHM. For example, for the Fe 3p spectra of the uncapped samples, literature suggested a metallic peak contribution at a binding energy of approximately 52.8 eV together with an unresolved peak representing higher oxidized states shifted to a higher binding energy than the metallic peak [27, 28]. Thus, the curve fitting of these spectra posed a trivial task, consisting of adding two peak features to the background model to obtain the final peak model.

On the other hand, the Ni $2p_{3/2}$ spectra of Permalloy found in the litterature suggested peak contributions from up to four individual compounds: Ni, NiO, $Ni(OH)_2$, $NiFe_2O_4$ [29]. Considering that all of the suggested species are modeled with up to five peak components in their respective pure form Ni $2p_{3/2}$ spectra, the curve fitting of these spectra required some lengthy detective work. The fitting of the Ni $2p_{3/2}$ was performed by adding the most prominent peak components from metallic nickel and its proposed oxides from the literature, according to the area contribution in their respective pure form spectrum, tabulated by Biesinger et al. [30] while monitoring the reduced chi-squared
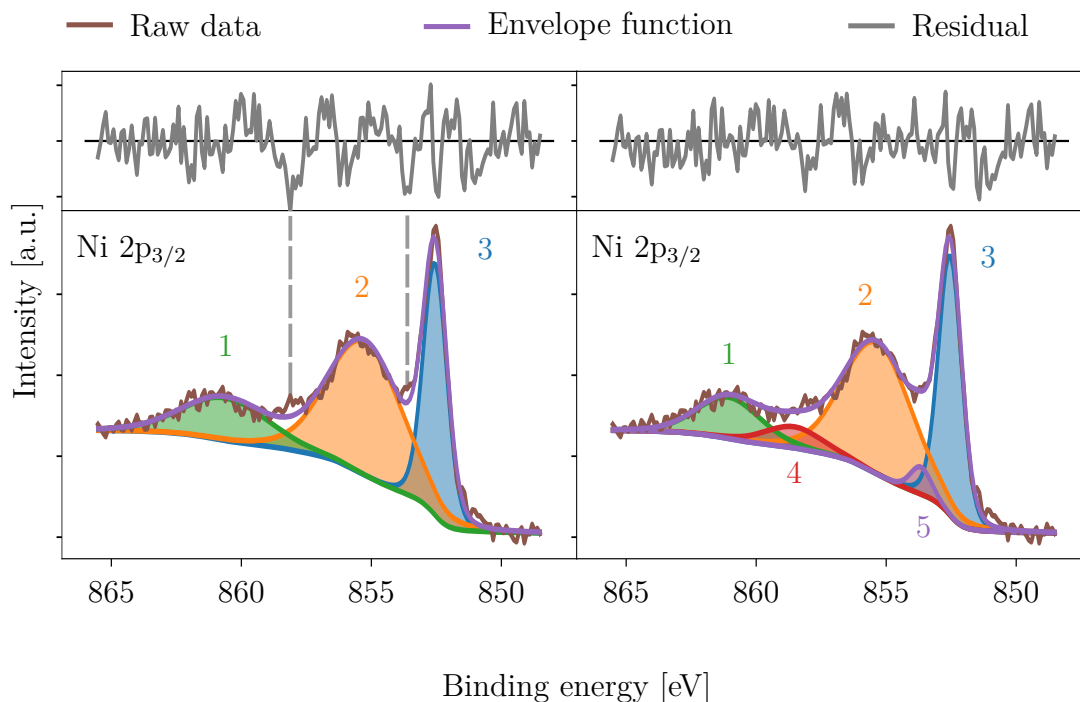
Figure 4.3: Goodness of fit assessment for the Ni $2p_{3/2}$ spectrum including three versus five peak components. The reduced chi-squared and Abbe parameters were improved by adding five peak components, indicated by a smaller residual. with respect to the peak model including three peak components.

and Abbe parameters. In fitting the individual peak components, the binding energy and FWHM were allowed to vary with ±0.1 eV from the tabulated values for an initial fit. Subsequently, the peaks that were restricted by the FWHM and binding energy range were allowed to float until they settled at parameters fitting the experimental data.

An example of two different peak models fitted to the Ni $2p_{3/2}$ spectrum of the uncapped control sample is shown in figure 4.3. When adding peak components to the peak model the residual of the envelope function was used as an instructive tool to identify the regions of the spectrum with a poor fit. In the spectrum fitted with three peaks, there were especially two points at which the envelope function failed to match the experimental data, as indicated by the dashed grey lines in figure 4.3. Adding two more peak components to the peak model resulted in a more evenly spread residual, yielding an improved Abbe score from 0.49 to 0.60 and a reduced chi-squared value from $\chi = 1.1$ to $\chi = 0.94$. The goodness of fit evaluation was performed on all the curve-fitted spectra presented in the results section. However, for the sake of readability, the fitted spectra will be presented without the residuals.

4.4 VSM measurements

The VSM measurements were performed using a Quantum Design PPMS VersaLab instrument with a VSM module. Prior to the measurements, the samples were mounted to a glass sample holder with a non-magnetic epoxy using a mounting stage to ensure correct positioning of the sample. Measurements were then initialized by performing a detection sequence in which the magnetic field was set to 2000 Oersteds (Oe) while the sample was vibrated and lowered through the detection coil. The sample position was then determined from the position for which the strongest magnetic signal was obtained. Measurement sequences were run by ramping the magnetic field linearly between a positive and negative field value for which the magnetization of the sample was fully saturated. Due to the various coercive field strengths of the individual samples, different field intervals were used to ensure that the magnetization of the samples was fully saturated. The increments of the magnetic field were set to 0.3 Oe/s together with an averaging time of 1 second, yielding an acceptable amount of noise.

Table 4.2: VSM measurement parameters.

Parameter	Value
Magnetic field interval	$H \in [-40, 40]$ Oe
Averaging time	1 s
Field increments	$\Delta H = 0.3$ Oe
Temperature	300 K
Pressure	~ 50 Torr

Savitsky-Golay data filtering

The saturated magnetic moment of the samples represented the parameter of most interest when probing the potential changes in magnetic characteristics of the samples. However, the raw data obtained from the VSM system contained a substantial amount of noise, causing the saturated tails of the measured hysteresis loops to be cluttered with random noise. Therefore, to determine the saturated magnetic moment of the samples, a Savitsky-Golay (S-G) filter was applied to smooth the experimental data. An S-G filter applies a local least-square fit to data points inside a specified *window length* using a polynomial of n-th degree. The filter algorithm then evaluates the fitted polynomial at the datapoint in the middle of the specified window.
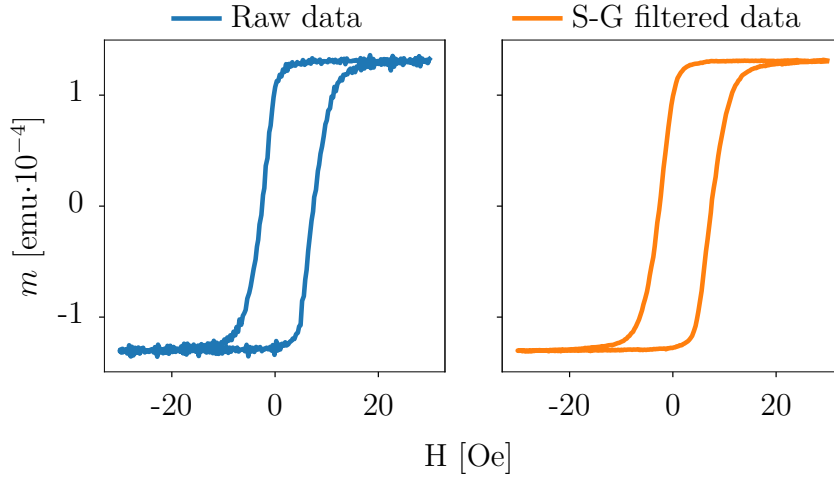
Figure 4.4: Raw VSM data and a corresponding filtered dataset using an S-G filter with first order polynomial and a window length of 9 data points.

In processing of the experimental VSM data, the NumPy function `numpy.signal.savgol_filter` with a polynomial of first order and a window length of 9 datapoints was found to produce sufficiently smoothed hysteresis loops. An example of a raw VSM measurement and the corresponding filtered dataset is shown in figure 4.4. With smoothed saturated tails of the measured hysteresis curves, the saturated magnetic moment, m_S could be determined by averaging the maximum and minmum magnetic moment of the filtered data $m_{\max}, m_{\min}$:

$$m_S = \frac{m_{\max} + |m_{\min}|}{2} \quad \text{emu.} \tag{4.1}$$

The magnetic moment of the various samples will be given in terms of m and m_S, in units of emu.

Determining oxide thickness from saturated magnetic moment

Due to the small dimensions of the nanomagnets constituting ASI systems, the thickness of the oxide scale forming on a nanomagnet could potentially make up a substantial fraction of its total volume. Therefore, an attempt was made to determine the oxide thickness of the oxide scale forming on an unprotected Permalloy surface from the saturated magnetic moment of the various fabricated samples.

Measurements were performed on uncapped samples with deposited film thicknesses of 10 nm, 20 nm, and 40 nm, subjected to plasma, hotplate, and the ambient atmosphere. Three samples were measured at each film thickness for each experimental group. Additionally, to investigate the protective capabilities of the aluminum capping layer, a set of capped samples subjected to the same

experimental treatments were measured to study potential differences in the saturated magnetic moment from that of the uncapped samples. The three data points for the saturated magnetic moment for each experimental group at various film thicknesses were then used in linear interpolation, allowing to extrapolate the intercept of the regression line and the y-axis.

Two assumptions were made to estimate the oxide thickness of the uncapped samples: first, it was assumed that a non-magnetic oxide, contributing with zero magnetic moment to the saturated moment, forms on the Permalloy surface, which consumes a finite amount of the metal. Secondly, it was assumed that the saturated magnetic moment of the samples was linear in the film thickness, $m_S \propto t_{\text{Oxide}}$. With these assumptions, the interpolation of the saturated magnetic moment versus film thickness would intersect the y-axis, representing the saturated moment, at the origin in the case of a pure metallic and magnetic sample. Following this argument, a potential decay in the saturated moment would be represented by a downward shift of the regression line, intercepting the y-axis at a value $-\delta m$. The downward shift of the regression line can be regarded as a loss of magnetic moment, which is related to the amount of consumed metal. Using the assumption that the oxide thickness is directly related to the amount of consumed metal, the oxide thickness can be estimated using:

$$t_{\text{Oxide}} = t_{\text{Metal}} \left(1 - \frac{m_S}{m_S + \delta m} \right) \tag{4.2}$$

where t_{Metal} is the thickness of the magnetic film as deposited and m_S is the measured saturated moment of the sample.

Noise assessment

To rule out possible sources of error in the VSM measurements, the noise in the VSM system was determined. The inherent noise of the system was assessed by running a measurement without the sample holder inserted in the measurement chamber and ramping the magnetic field between ± 10 Oe. The rest of the parameters used correspond to the parameters used in measurements of the samples, given in table 4.2.

Additionally, the residual between an S-G filtered dataset and the raw data was assessed by subtracting the filtered data from the experimental data. The results of the measurement of the system noise and the S-G filter residuals for a test sample, are given in table 4.3.

The noise measurements revealed that the average moment for the VSM system was shifted slightly to negative values, which might indicate poor calibration of the VSM module. However, the shift is several orders of magnitude lower than the signal obtained for the various fabricated samples and can thus be considered

Table 4.3: Results of the noise assessment performed on the VSM system, iuncluding the average magnetic moment m_{avg} and the root mean squared error (RMSE).

Measurement	m_{avg} [emu]	RMSE [emu]
System noise	$-3.8 \cdot 10^{-7}$	$2.3 \cdot 10^{-6}$
S-G filter residual	$6.1 \cdot 10^{-10}$	$2.5 \cdot 10^{-6}$

negligible. The residuals of the filtered dataset were found to exhibit similar to the inherent noise of the system. This observation led to the assumption that the uncertainty in the saturated magnetic moment determined from the filtered datasets was comparable to the RMSE of the system noise.

4.5 On anisotropy in Permalloy thin films

Initial measurements of the uncapped Permalloy samples led to qualitatively different hysteresis curves for samples originating from the same batch. Therefore, the question was raised whether there was an inherent magnetic anisotropy in the fabricated samples, as the samples originating from the same wafer should behave identically. Having scribed the samples into square chips of $4\,\mathrm{mm} \times 4\,\mathrm{mm}$, a degree of freedom that potentially could cause the observed difference in magnetization dynamics was the sample orientation. Therefore, after performing an initial measurement on a sample, a subsequent measurement was performed in which the sample was rotated by 90° with respect to the initial measurement.

The apparent magnetic anisotropy was investigated in greater depth by consulting the transmission electron microscopy (TEM) group at NTNU to investigate potential structural anisotropy of the samples leading to magnetic shape anisotropy. TEM samples were fabricated by depositing Permalloy onto a TEM grid and subsequently imaged as-grown using the brightfield TEM imaging mode. The TEM images were then analyzed using a Fast Fourier transform (FFT) algorithm to investigate structural anisotropy in the original images.

A completely isotropic grain structure would result in a perfectly symmetrical image in the Fourier space as the symmetry of the Fourier transform reflects the symmetry of the original image [31]. Therefore, anisotropy in the images could be quantified by curve-fitting an ellipse to the center, corresponding to the low-frequency region, of the transformed images. The eccentricity of the fitted ellipses could then be extracted as a measure of deviation from a perfectly symmetric circle, corresponding to an inherent anisotropy in the original TEM images. The eccentricity of an ellipse, e, is equal to the distance from the origin to the focal point and can assume values between 1 and 0 and one where $e = 0$ corresponds to a perfect circle, shown in figure 4.5. The orientation of the fitted
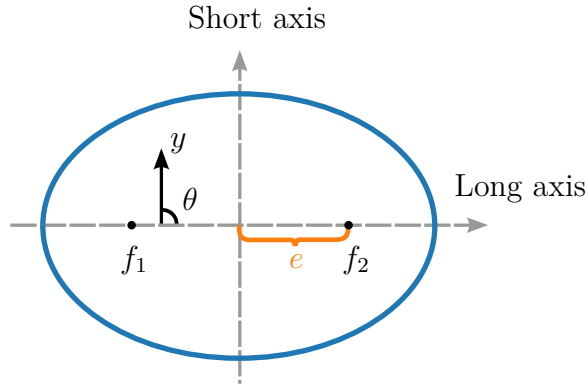
Figure 4.5: The eccentricity, e, of an ellipse is defined as the distance from the origin to the focal points, f_1, f_2. The orientation of the ellipse can be given in terms of the angle θ, between the long axis of the ellipse and the vertical y-axis.

ellipses also yielded information about the symmetry in the transformed images, which could be extracted from the angle θ, defined as the angle between the long axis of the ellipse and the vertical y-axis.

Before performing the Fast Fourier transform of the original TEM images, a vignette was applied using a gaussian blur on the edges of the image to reduce edge effects in the resulting FFT. The FFT was then applied using the 2D discrete Fourier transform function from the NumPy library. Subsequently, a contrast limited adaptive histogram equalization (CLAHE) algorithm was used to increase the contrast of the FFT images. Fitting ellipses to the most intense areas in the low-frequency region of the FFT was performed first by producing a binary mask of the FFT. The binary masks were generated by setting the pixels of the FFT image to 0 or 255 according to an intensity threshold value. The threshold values were decided based on a multi-otsu-thresholding algorithm, grouping the pixels into classes according to the intensity of the gray levels in the image. Having produced binary masks outlining the low-frequency regions of the FFT, curve fitting was performed using the OpenCV library to identify the contours of the binary mask and subsequently fit an ellipse to the detected contours. The fitted ellipses yielded eccentricity values and the angle θ, which could then be used to assess the degree of asymmetry in the FFT, corresponding to structural anisotropy in the TEM images. A flow chart representing the image processing performed on the TEM images is shown in figure 4.6 and the functions applied in the various steps are listed in table 4.4. The script used in the image processing is given in appendix E.

Original image   Vignette

FFT   CLAHE

Binary masks

Multi-Otsu
thresholding   Curve fitting
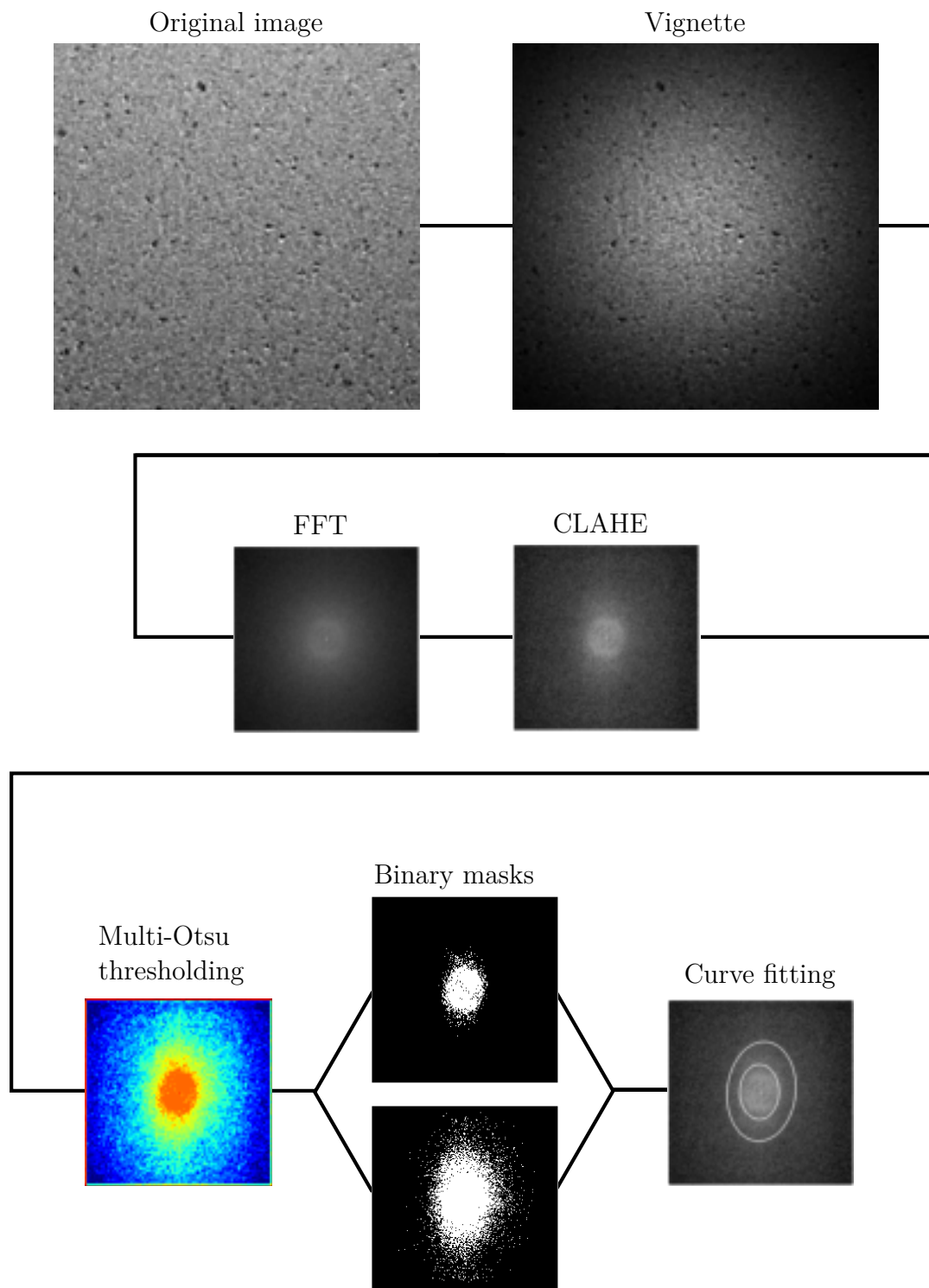
Figure 4.6: Flowchart of the image processing performed on the brightfield TEM images.

Table 4.4: Functions used in the image prosessing steps of the TEM images.

Processing step	Applied function
Vignette	`cv2.getGaussianKernel`
FFT	`numpy.fft.fft2`
CLAHE	`cv2.createCLAHE`
Multi-Otsu thresholding	`skimage.filters.threshold_multiotsu`
Binary masks	`cv2.threshold`
Curve fitting	`cv2.findContours`
	`cv2.fitEllipse`

5 | Results and Discussion

In the following chapter, the results obtained from the experimental work will be presented and discussed. Firstly, the XPS results will be presented to establish the chemical composition of the various samples. Secondly, the VSM results and TEM image analysis concerning the magnetic anisotropy in the Permalloy samples will be presented. Subsequently, the VSM measurements performed on the treated samples and estimated oxide thicknesses are presented before a general discussion on the relevance and implications of the findings is given.

5.1 Chemical composition of sample surfaces

This section will present the processed XPS data for the capped and uncapped samples in the stated order. First, the wide scans will be presented to provide an initial notion of the differences between the XPS spectra for the experimental groups. Subsequently, the detailed scans deemed most relevant for the capped and uncapped samples will be presented. For the capped samples, these include the Al 2p and Ni $2p_{3/2}$ spectra, while for the uncapped samples, the Ni $2p_{3/2}$ and Fe 3p spectra will be given. For ease of reference, the Ni $2p_{3/2}$ spectrum will be referred to as Ni 2p throughout the rest of the thesis. All the fitting parameters used in the various peak models are given in appendix C.

5.1.1 Capped samples

The wide scans performed on the capped control, hotplate, and plasma samples plotted on an arbitrary unit scale are shown in figure 5.1. In the figure, the most prominent peak features are labeled and indicated by the dashed lines, including the Ni 2p, Fe 2p, Ni LMM auger peak, O 1s, C 1s, Al 2s, and Al 2p peaks. Comparing the three wide scans qualitatively, we observe that they exhibit mostly the same features at the same binding energies except for two emerging peaks in the plasma wide scan, appearing at approximately 685 eV and 832 eV binding energy, indicated by the shaded green rectangles in figure
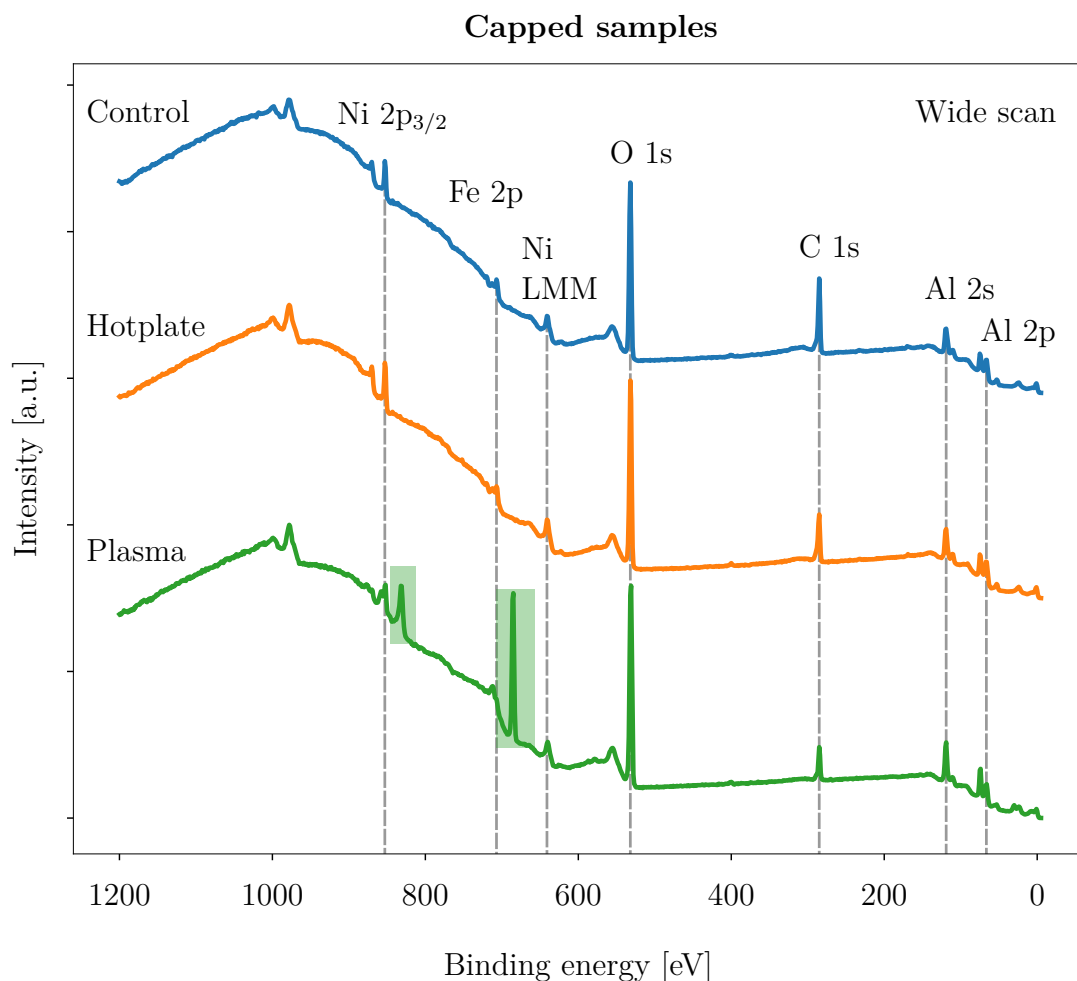
Figure 5.1: Wide scans performed on the capped Permalloy samples where the peaks of interest, and other prominent peaks, are labeled and indicated by dashed lines. The individual scans were normalized and shifted with respect to each other for visualization purposes. The peaks shaded in green rectangles were found exclusively in the spectrum of the plasma sample and are assumed to be caused by fluoride contamination of the plasma cleaner.

5.1. Peak detection in CasaXPS yielded relatively good fits for the two peaks with the fluoride 1s and the fluoride KLL binding energies of 686 eV and 840 eV, respectively. Literature also provided tabulated values for binding energies of F 1s and F KLL of 685 eV and the KLL peak at 832 eV, almost identical to the obtained binding energies for the unidentified peaks [21]: This strongly suggests the presence of fluoride on the surface of the plasma-treated sample. In addition, a relatively small peak located near that of the F 1s binding energy was also found in the widescan for the uncapped plasma sample, indicated by the green rectangle in figure 5.3. Therefore, considering that the fluoride signal was obtained exclusively for the plasma-treated samples points toward possible

fluoride contamination of the plasma cleaner.

The curve fitted Al 2p spectra, and the background-subtracted Ni 2p spectra obtained for the capped samples are shown in figure 5.2. The best peak model found for the Al 2p spectra of the control and hotplate samples included peak components from two spin-split metallic Al peaks, Al $2p_{1/2}$ and Al Al $2p_{3/2}$, and two additional peaks corresponding to the oxides Al_2O_3 (alumina) and AlO_x. The spin split metallic peaks were fitted with a spacing of 0.4 eV and 0.6 eV for the control and hotplate sample, respectively, which is in close agreement with online XPS libraries reporting a spin splitting of the Al 2p energy level of approximately 0.44 eV [32].

The majority of the Al 2p spectra found in the literature were found to be fitted with a single metallic Al peak and an alumina peak. This peak model was attempted fitted to the experimental data, but a superior fit was obtained by including the spin-split Al 2p peaks and the AlO_x peak in the model. Comparing the Al 2p spectra of the control, hotplate, and plasma samples, there is a clear trend of a decreasing metallic Al signal from the control sample, through the hotplate sample to the plasma sample, where the metallic signal is completely absent. The absence of metallic Al in the spectrum of the plasma sample strongly suggests that the Al within the sampling depth of the XPS is fully oxidized.

More information about the degree of oxidation for the capped samples could be inferred by considering the Ni 2p spectra. Due to a relatively large amount of noise in the Ni 2p spectra, the spectra were only background subtracted and plotted above one another for visualization purposes. Most noteworthy when considering the Ni spectra is the fact that a significant metallic nickel signal was obtained for all the samples with a well-defined Ni $2p_{3/2}$ peak with a binding energy of ~ 852 eV. Assuming an abrupt separation of Al capping and the underlying metallic Permalloy layer, the obtained spectra indicate that the sampling depth of the XPS exceeds the thickness of the capping layer of 2.5 nm.

Considering the Ni 2p spectrum obtained for the plasma sample, we observe an increased signal for higher binding energies which qualitatively separates it from the control and hotplate spectra. Without a peak model for the Ni 2p spectra, the specific compound giving rise to the observed signal is not determined; however, the observed signal resembles a chemical shift found for oxidized states. This observation indicates that the plasma treatment performed on the capped sample was able to fully oxidize the 2.5 nm aluminum film and further induce an internal oxidation reaction of the underlying metallic Permalloy. The spectra obtained for the control and hotplate samples bear a stark resemblance to the metallic nickel 2p spectrum, characterized by a well-defined $2p_{3/2}$ peak at approximately 852 eV and two mellow satellite peaks shifted by approximately
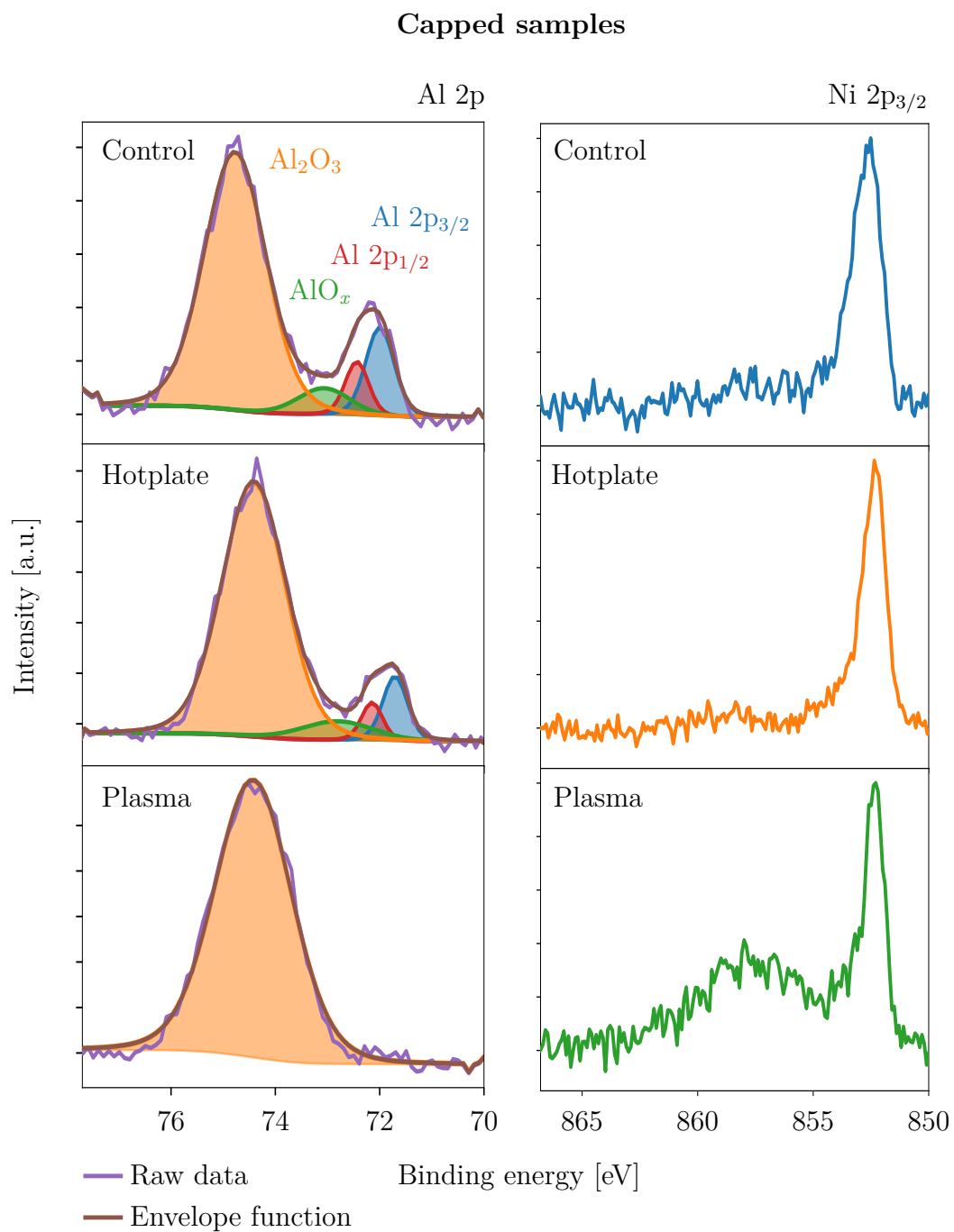
Figure 5.2: Curve fitted Al 2p$_{3/2}$ and background subtracted Ni 2p$_{3/2}$ spectra for the capped hotplate, plasma and control samples. The peak components in the curve fits of the Al 2p spectra and their corresponding chemical species are related by the same coloring.

3.7 and 6 eV towards higher binding energies [30]. This similarity indicates that the capping layer was able to fully protect the base metal under ambient conditions and elevated temperatures up to 100 C°.

Sources in the literature state that Al forms a native oxide layer that self-terminates at a thickness of about 1-2 nm in a low-temperature regime, $T < 573$ K [33, 34]. These findings agree with the XPS results for the control and hotplate samples if we assume that the Ni 2p spectra of the two are purely metallic. In the assessment of a purely metallic nickel signal, it would have been instructive to perform ion milling on an uncapped sample for reference, but due to limited availability of the XPS instrument, this procedure was not performed.

5.1.2 Uncapped samples

The wide scans of the uncapped samples are shown in figure 5.3, where the relevant peaks are labeled and indicated by dashed lines. From the figure, we observe that the wide scans appear relatively similar, differing mainly in peak intensity of the O 1s and C 1s peaks. Similar to the wide scan performed on the capped plasma samples, the uncapped plasma sample also showcased a minor peak feature corresponding to the F 1s binding energy, indicated by the shaded rectangle in figure 5.3.

The curve fitted Ni 2p, and Fe 3p spectra for uncapped samples are shown in figure 5.4, where the chemical compound assigned to the individual peak components and their respective chemical formula are indicated by the same coloring. Different species were included in the peak models implemented for the various Ni 2p spectra to obtain a good fit to the experimental data and an acceptable reduced chi-squared value. The spectrum obtained for the control sample was fitted with a prominent Ni $2p_{3/2}$ peak with peak binding energy 852.5 eV together with the characteristic 6 eV Ni satellite [30]. In addition, three separate NiO peaks were fitted to the spectrum based on the tabulated peak binding energies in the Ni 2p spectrum for pure NiO, tabulated by Biesinger et al. [30].

Regarding the spectrum obtained for the hotplate sample, the first and second NiO peaks indicated with green and orange shading, respectively, were fitted with an increased area contribution relative to the metallic nickel peaks, while the third NiO peak, colored in purple, was deemed superfluous by the curve fitting algorithm. Instead, the hotplate sample was fitted with an emerging peak with a binding energy ~ 854.4 eV associated with $NiFe_2O_4$. Lastly, the Ni 2p spectrum of the plasma sample exhibited zero contribution from the metallic peak components, with an increased signal for the prominent NiO peaks and the $NiFe_2O_4$ peak. Lastly, considering the peak models of the Ni 2p spectra of Permalloy, several sources in the literature were found to include peaks associated

Uncapped samples
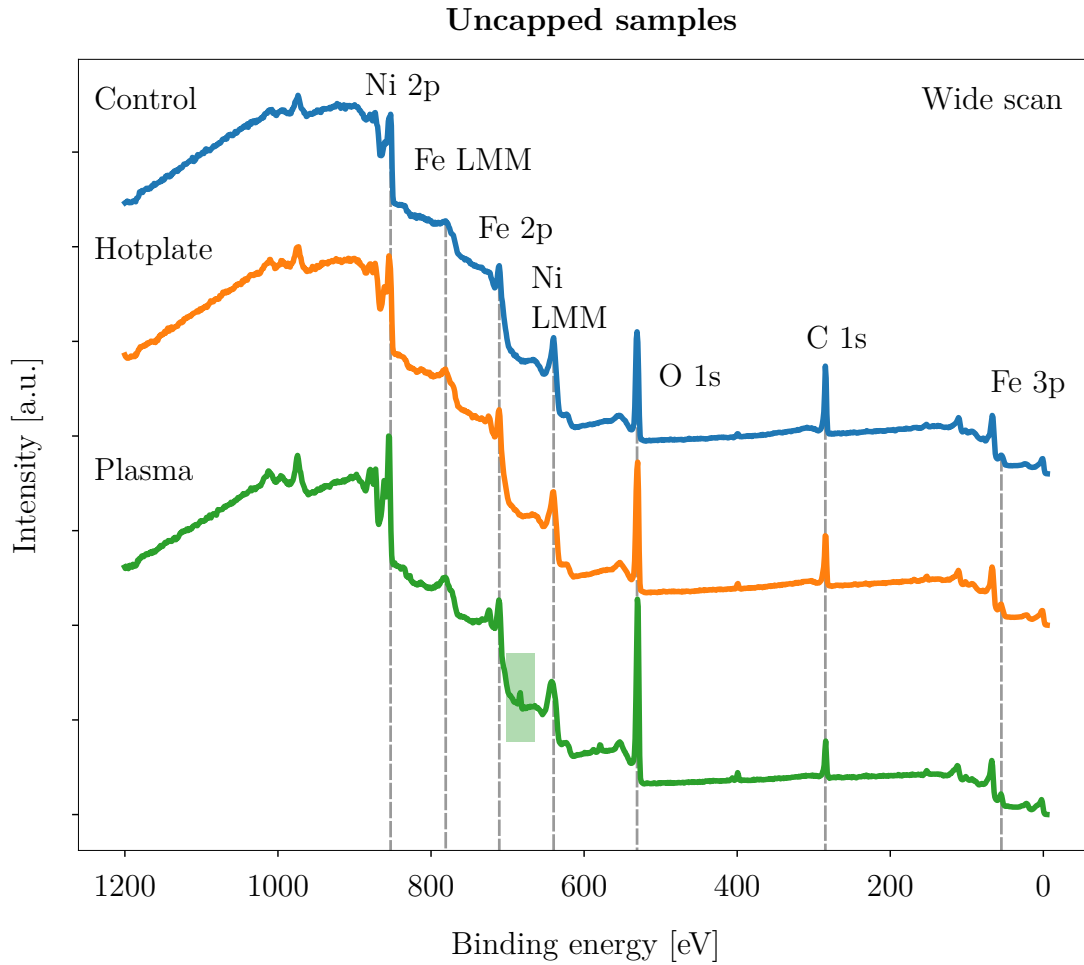
Figure 5.3: Wide scans performed on the capped Permalloy samples where the peaks of interest, and other prominent peaks, are labeled and indicated by dashed lines. The individual scans were normalized and shifted with respect to each other for visualization purposes. The small shaded peak feature in the spectrum of the plasma sample is found exclusively for the plasma sample and is presumably caused by fluoride contamination of the plasma cleaner.

with $Ni(OH)_2$ in similar XPS spectra [35]. However, including these peaks did not improve the goodness of fit to the experimental data in this work.

Similar work concerning the oxidation of Permalloy thin films performed by Fitzsimmons et al. is in relatively good agreement with the trends observed in the Ni 2p spectra of the uncapped samples [36]. In the work of Fitzsimmons, the chemical and magnetic characteristics of uncapped Py surfaces were investigated as a function of thermal annealing. The authors claim that oxidation of the Py surface proceeds by forming a NiO layer on top of a Ni-Fe-oxide layer, which is in contact with the metallic Permalloy. Regarding the oxidation kinetics of the different oxide layers, the authors state that the thickness of the outermost

NiO layer stays constant with annealing time, while the Ni-Fe-oxide layer grows at a parabolic growth rate upon thermal annealing. These results can possibly explain the appearance of the $NiFe_2O_4$ peak obtained for the hotplate and plasma samples, which both have been subjected to elevated temperatures.

When it comes to the Fe 3p spectra for the uncapped samples, the experimental data featured a relatively low signal-to-noise ratio, which affected the quality of the curve fitting. The peak models implemented consisted of a metallic iron peak (Fe) and an unresolved peak component, representing the higher oxidation states of iron, Fe_3^+ and Fe_2^+. The metallic peaks of the control and hotplate samples were fitted at 52.7 eV and 52.8 eV, respectively, in close agreement with the tabulated value of the Fe 3p binding energy of 52.8 eV [28]. Similar to the Ni 2p spectra presented, the Fe 3p spectrum of the plasma sample was fitted with zero contribution from the metallic iron peak component. The unresolved oxide peaks were fitted with peak binding energies of 55.3 eV, 55.5 eV, and 55.1 eV for the control, hotplate, and plasma sample, respectively. Tabulated peak binding energies for the iron oxides Fe_3^+ and Fe_2^+ of 55.6 eV and 53.7 eV found in the literature both fall in under the unresolved oxide peak for in the various spectra [37]. Considering that the unresolved peak for both the control and hotplate samples were fitted with a center of mass closer to that of the tabulated Fe_3^+ peak suggests a greater contribution from 3^+ oxidized iron to the obtained XPS signal.

The main oxides of iron corresponding to the Fe_2^+ and Fe_3^+ oxidation states are Fe_2O_3 and Fe_3O_4 respectively, occuring in various phases with different structural and magnetic properties [38]. Therefore, it can be assumed that, predominantly, the concentration of Fe_3O_4 increases from the control sample to the hotplate and the plasma samples. In hindsight, the Fe 2p spectrum, regarded as the primary XPS spectrum of iron [21], could have been scanned in favor of the Fe 3p spectrum to obtain a better signal-to-noise ratio, allowing for a more detailed curve fitting process enabling discrimination of contributing species in the spectra.

The XPS results obtained for the uncapped samples originating from the first and second fabricated batches are shown in figure 5.5, in which there is an appreciable difference in the signals for the samples fabricated two weeks apart. More specifically, batch one was fabricated on March 8th, while the second batch was fabricated on March 22nd. The XPS measurements on the uncapped samples were performed on March 29th. This being said, there is clear evidence that the oxidation reaction of the unprotected samples does not self-terminate over a period of three weeks and that a period of two weeks of prolonged exposure to the oxidizing atmosphere is able to produce an observable difference in the chemical composition of the sample surface. The curve fitted spectra in figure 5.5 suggest a larger contribution from the oxidized states for the sample originating

Uncapped samples

Ni 2p$_{3/2}$ Fe 3p
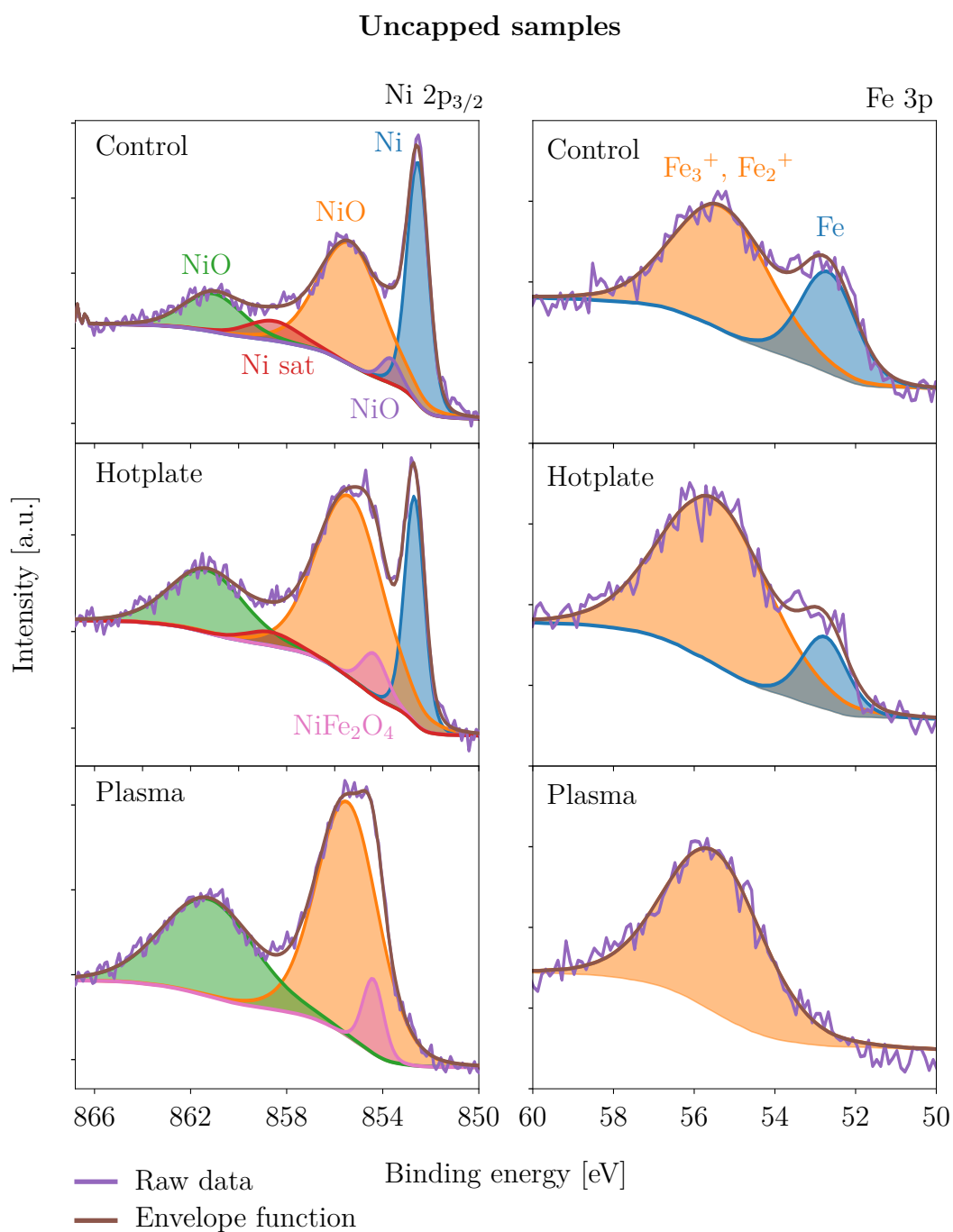
Figure 5.4: Curve fitted Ni 2p$_{3/2}$ and Fe 3p spectra for the uncapped hotplate, plasma and control samples. The peak components in the two spectra and the assigned chemical species are indicated by the same coloring.
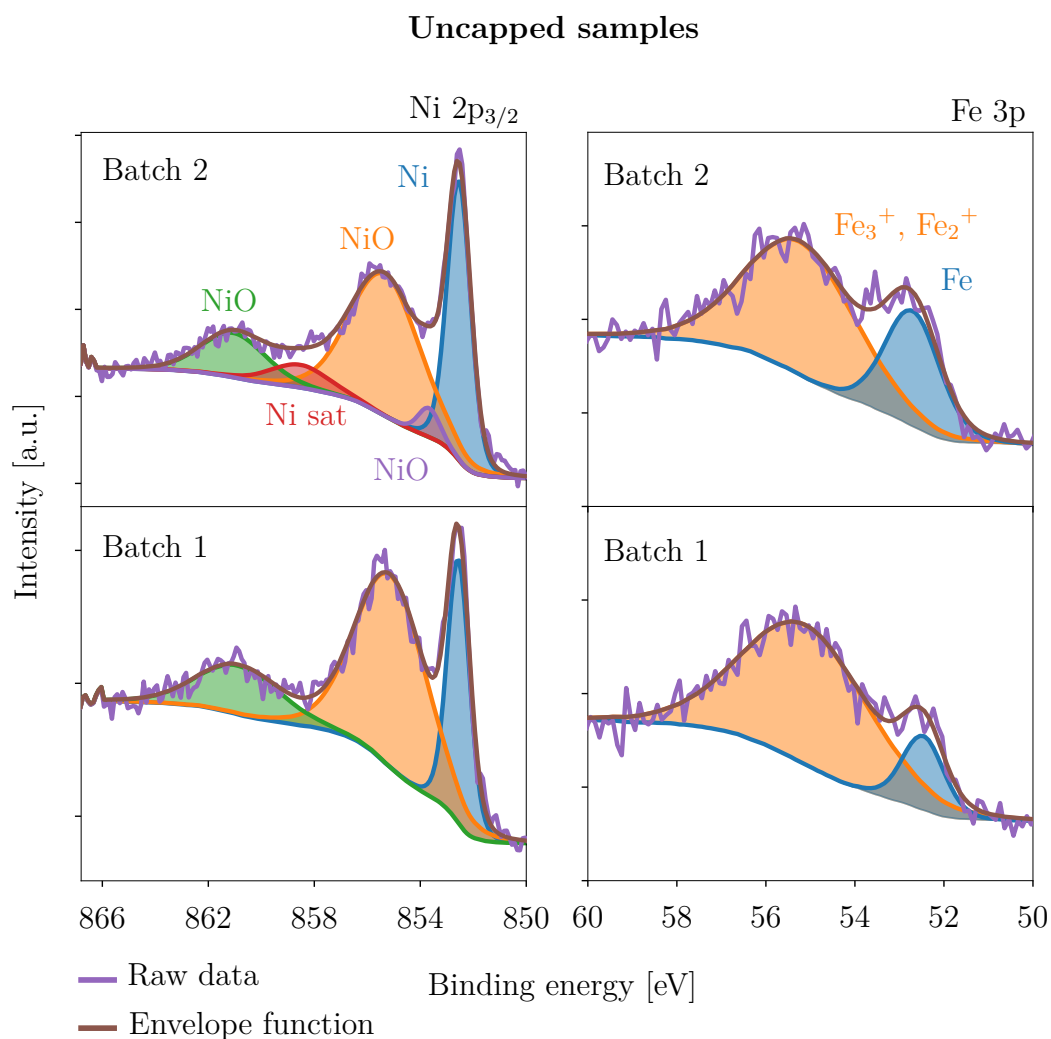
Uncapped samples

Figure 5.5: Curve fitted Ni $2p_{3/2}$ and Fe 3p spectra for the uncapped control samples from the first and second fabricated batch. The peak components in the two spectra and the assigned chemical species are indicated by the same coloring.

from the first batch in both the Ni 2p and Fe 3p spectra. Comparing the spectra of the batch 1 sample with the curve fitted spectra in figure 5.4, there is a strong resemblance to the curve peak model obtained for the hotplate sample except for the absence of the $NiFe_2O_4$ peak component. This observation also supports the claim that the $NiFe_2O_4$ forms under elevated temperatures.

Although there are many pitfalls in the process of assigning chemical species to fitted peak components of an XPS spectrum, it will be assumed, from this point on, that the various chemical species assigned to the XPS spectra are *de facto* present on the sample surfaces to facilitate the following discussion.

5.2   Anisotropy in Permalloy thin films

As indicated in the experimental section, initial measurements of the uncapped samples revealed a qualitative difference in the hysteresis loops obtained for samples originating from the same batch. Performing two subsequent measurements on each sample revealed that the same was true for the individual samples, as the obtained hysteresis loops differed qualitatively for 0° and 90° sample orientations.

The obtained anisotropy in the VSM measurements is shown in figure 5.6, featuring a selection of measurements performed on capped and uncapped samples originating from batch one and two. Considering figure 5.6 it is apparent that the majority of the samples exhibited a significant magnetic anisotropy, indicated by the different shapes of the obtained hysteresis curves for the respective orientations, while the two samples indicated with red frames exhibit a near-zero magnetic anisotropy. Arguably, the most noteworthy feature of figure 5.6 is that two of the samples exhibited a negligible degree of anisotropy, which indicates that there were appreciable sample-to-sample differences for samples originating from the same batch. The sample-to-sample differences suggest that some factor that has not been accounted for causes local differences between metal disks deposited on the same wafer.

When it comes to the shapes of the obtained hysteresis curves, the samples exhibiting anisotropy resemble hysteresis measurements obtained for uniaxially anisotropic systems with one easy and hard axis of magnetization. Work performed by Donald O. Smith reports that evaporated films of Permalloy have been found to exhibit uniaxial anisotropy with similar sample fabrication as the one used in this work [39]. Smith proposes several possible contributions to the observed uniaxial anisotropy, one of which is anisotropic strain in the magnetic thin film. This effect could potentially describe the obtained sample-to-sample differences in that the deposited films are mostly strained, causing the observed anisotropy, while in some local regions, the strain may have relaxed, leading to isotropic magnetic behavior.

Other work in the literature on magnetic anisotropy in the Permalloy material system suggests various methods to induce magnetic anisotropy in the material. Examples are magnetic annealing during metal deposition, thermal annealing, or performing metal deposition at an oblique angle [40]. Here, it is worth emphasizing that the electron beam, responsible for the evaporation of the Permalloy metal, is focused on the target material by applying a magnetic field, which potentially could have induced anisotropy in the deposited metal. However, as the samples were rotated during metal deposition, this effect should be canceled out. The possibility of an induced anisotropy due to metal deposition at an oblique angle is also present, although angles of incline used to induce an
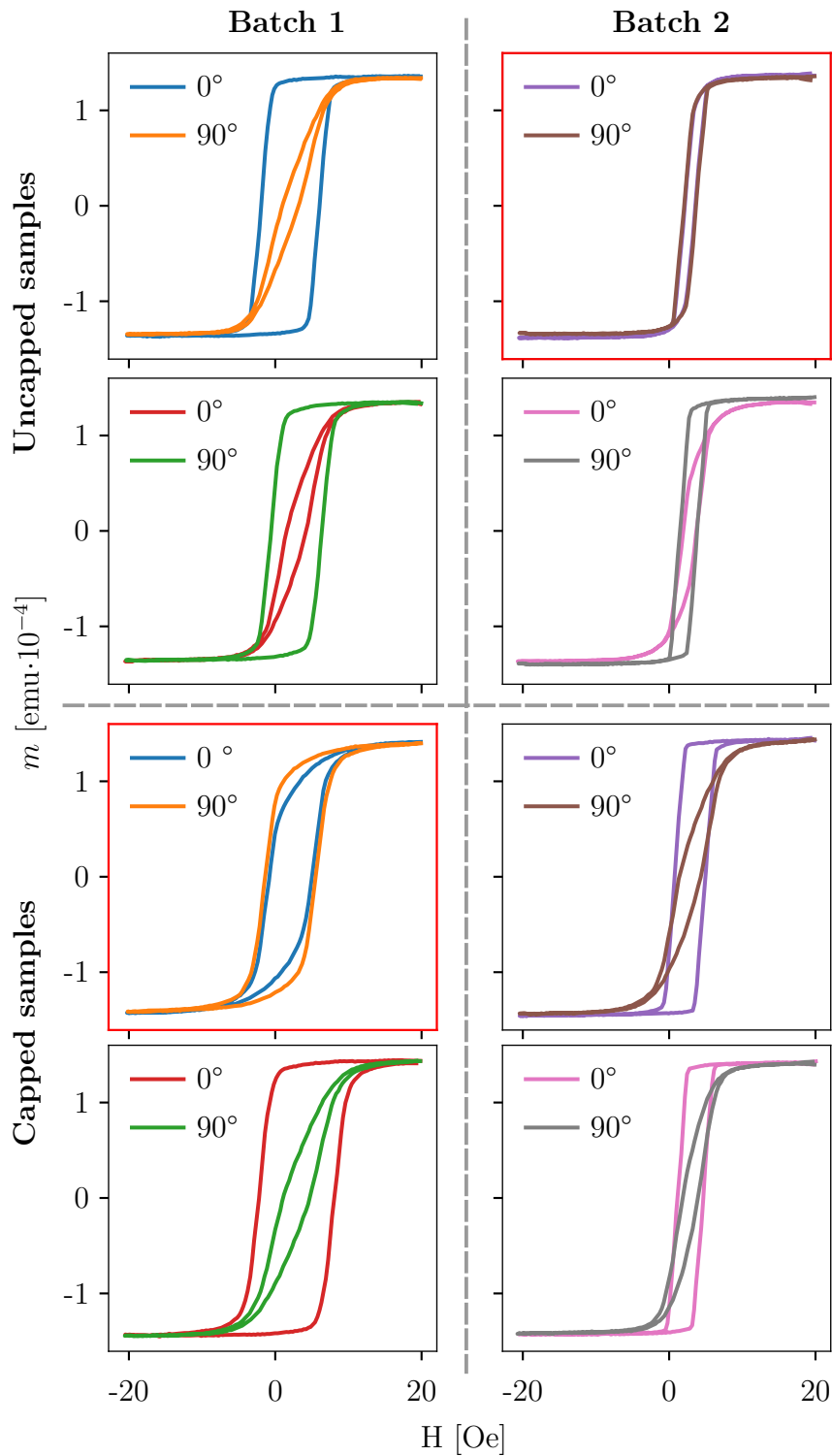
Figure 5.6: Comparison of filtered hysteresis data for a selection of samples from the first and second batch. The majority of the samples exhibit a clear anisotropy, indicated by the different shapes of the curves at 0° and 90° rotation of the samples. The two measurements indicated by red frames exhibit a near zero anisotropy.

observable anisotropy in the literature are reported to be in the range between 40°-50°, which is considerably larger than an incline caused by an uneven mounting of the wafer during metal deposition.

In the light of the chemical analysis performed on the uncapped Permalloy samples, it is interesting to consider the implications of magnetic coupling between the AF NiO layer and the underlying FM Permalloy. For example, Prosen et al. argued that the presence of NiO on metallic Permalloy is able to induce a rotatable anisotropy, where the easy axis of magnetization can be set by applying a sufficiently strong magnetic field [41]. The authors further propose that magnetic interactions between AF NiO and the underlying nickel-rich FM layer can produce magnetic hysteresis measurements with a unidirectional anisotropy, similar to the measurements obtained in this work.

Considering the strong NiO signal obtained for the uncapped samples, the possibility of a coupling between the AF nickel-oxide and the underlying FM Permalloy contributes to the observed magnetic anisotropy can't be excluded. However, the anisotropy was also found for the capped samples, which exhibited a zero signal for NiO at the sample surface. At the same time, the capped samples were fabricated with unprotected sidewalls as a consequence of the photolithography process, meaning that coupling of NiO and FM Permalloy could occur in this region. That being said, assuming there exists an exchange bias at the NiO/Py interface and considering the area of the sidewalls of the sample versus the in-plane surface area of the disks, the exchange bias should be much more pronounced for the uncapped samples. The fact that the capped and uncapped samples behaved similarly in magnetic measurements, therefore, suggests that the observed anisotropy may be ascribed to other effects than exchange biasing of the ferromagnetic material.

The image processing performed on the TEM images yielded additional information concerning the grain structure of the fabricated samples. Brightfield TEM images taken in two different windows, "window 1" and "window 3" of the TEM grid and their respective curve fitted FFTs are shown in figure 5.7 and 5.8, while the parameters extracted from the curve fitting are given in table 5.1.

Firstly, the brightfield TEM images in figure 5.7 with a resolution on the < 100 nm scale revealed well-defined grains of the Permalloy metal. From the insets in the TEM images, showing magnified versions of the highlighted white squares, we can also observe resolved grain boundaries for the Permalloy film. From visual inspection of the two images, it would appear that there is no preferred directionality in the grain structure. However, the curve fitting of the FFTs yielded a more nuanced picture as the FFTs resulting from both TEM images in the figure 5.7 were fitted with ellipses featuring high eccentricities. The ellipses fitted to the most intense regions of the two FFTs yielded eccentricity

(a) Window 1
(top left)

80 nm

(c) Window 3

80 nm
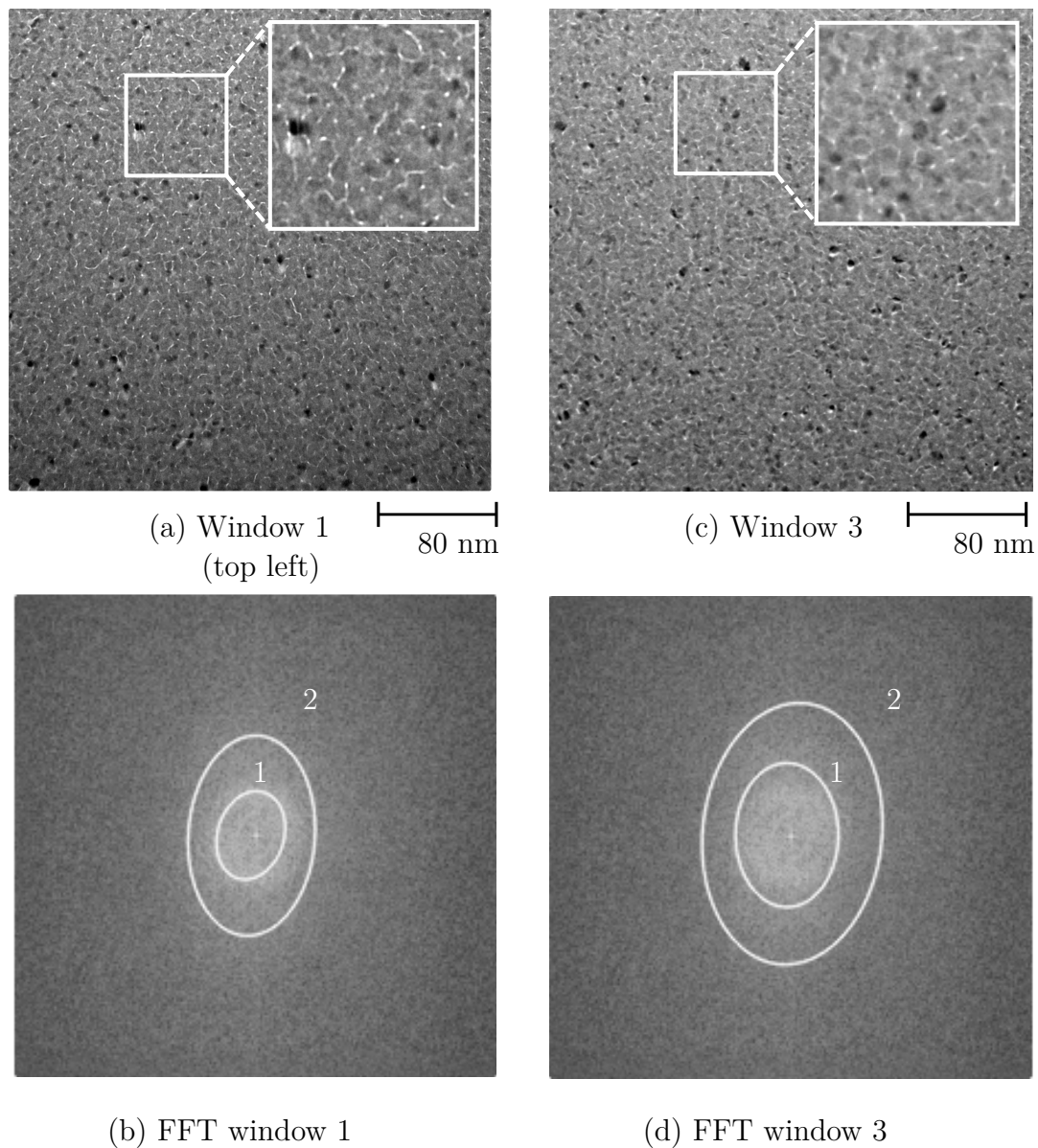
(b) FFT window 1

(d) FFT window 3

Figure 5.7: High resolution TEM images taken in (a) window 1 and (b) window 3 of the TEM grid and their corresponding curve fitted FFT images. The insets in (a) and (b) shows magnified versions of the areas indicated by the white frames. The fitted ellipses exhibit an appreciable eccentricity and similar orientations for both the Fourier transformed images.

(a) Window 1
(center)

80 nm

(b)
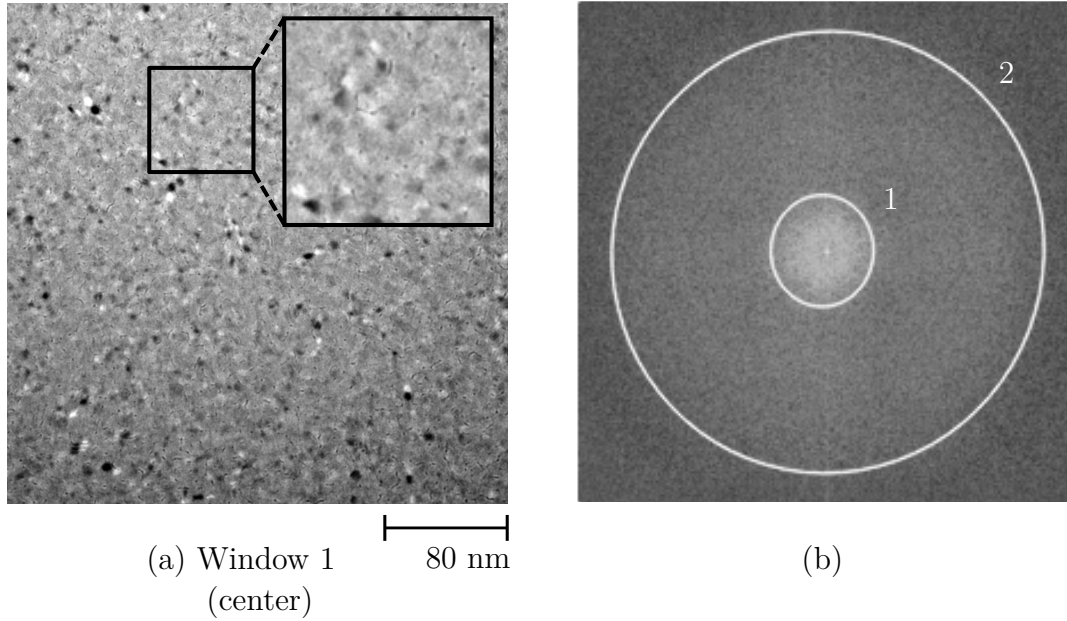
Figure 5.8: (a) Low-resolution TEM image taken in the center of window 1 of the TEM grid and (b) the corresponding curve fitted FFT image. The inset in (a) shows magnified versions of the area indicated by the black frame. The fitted ellipses exhibit relatively low eccentricity and directionality.

of approximately ~ 0.7 with similar orientations of the long axis between 0° and 16.9° along the vertical axis of the images. These findings suggest that there is an inherent asymmetry in the original TEM images, corresponding to a structural anisotropy of the grain structure.

In addition to the processing performed on the high resolution TEM images in figure 5.7, a second TEM image acquired in window 1 of the TEM grid was analyzed, shown in figure 5.8 (a). The original TEM image was taken in the center of the first window and featured a much lower resolution than the previously described images, making it practically impossible to distinguish the individual grains of the sample. In contrast to the curve fits of the FFTs obtained for the high-resolution images, the FFT of the low-resolution image was fitted with ellipses having significantly lower eccentricity. The inner and outer ellipses of the FFT was fitted with eccentricities of 0.36 and 0.17 and with angles $\theta_1 = 0.6°$ and $\theta_2 = 30.6$ respectively. Considering the low eccentricity and the discrepancy in the orientations of the ellipses, it can be inferred that there is a high degree of isotropy in the original TEM image.

Taking into account that the main difference between the analyses presented above is the fact that in the former, the grain structure was clearly resolved, whereas the opposite is true in the latter, strongly suggests that the image processing captures an inherent anisotropy in the grain structure of the sample.

Nonetheless, there are several sources of error in the image processing that should be addressed.

A possible source of error is attributed to the fact that the ellipses labeled with number 1, fitted to the lowest frequency region, appear to be shifted with respect to the origin for both window 1 and window 3 in figure 5.7. The shift of the ellipses indicates a possible artifact of the thresholding or contour detection steps, as an FFT should be symmetric with respect to the origin [31].

As a final remark on the magnetic anisotropy observed for the Permalloy samples, it should be emphasized that the measured anisotropy in the VSM measurements is relatively small, indicated by the minor difference in the coercive field, on the order of a few Oersteds, found for the easy and hard axis hysteresis loops. With regards to the nanomagnets constituting an ASI, the coercive field of a single nanomagnet is stated to be 46 mT in the work of Amanda Langørgen [42]. The stated switching field amounts to 460 Oe, assuming a non-magnetic medium, and reflects the strength of the shape anisotropy in the elongated nanomagnets in the ASI systems. Therefore, the observed anisotropy field, causing a difference in coercivity on the order of a few Oersteds, can be regarded as negligible when compared to the shape anisotropy of a nanosized Permalloy magnet.

Table 5.1: Parameters extracted from the curve fitting performed on the Fourier transformed TEM images.

TEM grid region	Ellipse number	e	θ
Window 1	1	0.67	16.9°
(top left)	2	0.77	4.2°
Window 3	1	0.70	0.0°
	2	0.73	6.2°
Window 1	1	0.36	0.6°
(center)	2	0.17	30.6°

5.3   Macroscopic magnetization

The saturated magnetic moment of the uncapped control, hotplate, and plasma samples for various film thicknesses are shown in figure 5.9 with the corresponding linear regressions of the saturated magnetic moment versus film thickness. The inset in the figure shows the extrapolated regression lines and the calculated y-intercepts, corresponding to the loss of magnetic moment δm. From the figure, we observe a trend of decreasing saturated moment, m_S, from the control samples to the hotplate and plasma samples, indicated by the downward shift of the
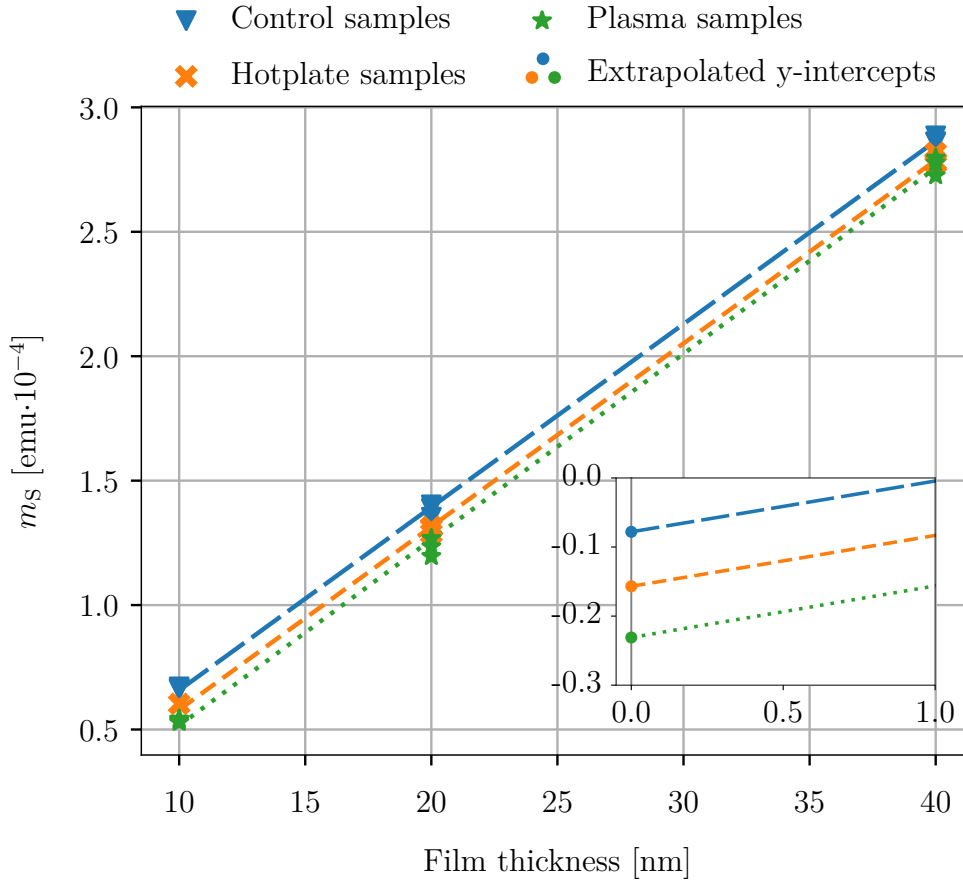
Figure 5.9: Linear interpolation of m_S for the various experimental groups plotted versus the film thickness. Three measurements make up the scattered values of the saturated moment for each experimental group at 10, 20 and 30 nm film thickness. The inset shows the extrapolated regression lines and their y-intercepts, corresponding to the loss of magnetic moment due to oxide formation, δm.

respective regression lines, which is assumed to be directly proportional to the oxide thickness for the various experimental groups.

Values for the average saturated moment m_S at 20 nm film thickness, loss of magnetic moment δm and the estimated oxide thickness t_{Oxide} together with the average saturated moment for the capped samples are given in table 5.2. The y-intercept, obtained by evaluating the respective regression lines at zero film thickness, yielded estimated oxide thicknesses of 1.1 nm, 2.1 nm, and 3.1 nm for the control, hotplate, and plasma samples, respectively, according to the assumptions made in the experimental section. These results agree relatively well with the work performed by Mattera et al., where the oxide thickness of uncapped Py samples treated to ambient atmosphere and oxygen plasma were reported to be 1.8 nm and 2.9 nm, respectively, obtained from x-ray reflectivity measurements [28].

Table 5.2: Average saturated magnetic moment for both capped and uncapped samples and loss of saturated moment and estimated oxide thickness for the uncapped samples.

Sample	m_S [emu]	δm [emu]	t_{Oxide} [nm]
Uncapped samples			
Control	$1.39 \cdot 10^{-4}$	$0.78 \cdot 10^{-5}$	1.1
Hotplate	$1.32 \cdot 10^{-4}$	$1.6 \cdot 10^{-5}$	2.1
Plasma	$1.26 \cdot 10^{-4}$	$2.3 \cdot 10^{-5}$	3.1
Capped samples			
Control	$1.51 \cdot 10^{-4}$		
Hotplate	$1.50 \cdot 10^{-4}$		
Plasma	$1.54 \cdot 10^{-4}$		
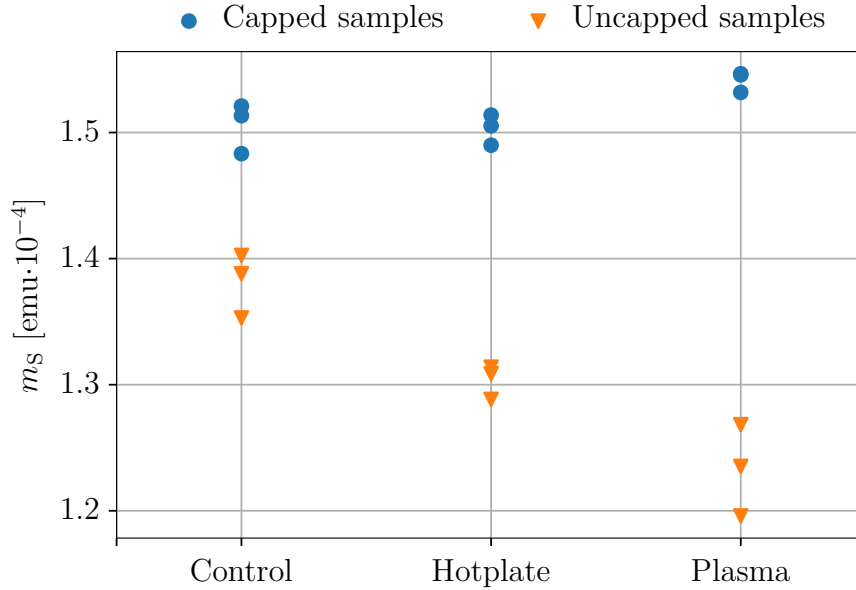
Figure 5.10: Scatterplot of the saturation magnetization for the capped and uncapped samples from the different experimental groups with a film thickness of 20 nm.

Figure 5.10 shows the saturated magnetic moment for the various experimental groups for the capped and uncapped samples with a metal thickness of 20 nm Py. In the scatterplot, the samples having received the same experimental treatment are plotted on the same vertical axis. From the figure, it is apparent that the saturated magnetic moment of the capped samples stays persistent between the samples belonging to different experimental groups, in contrast to the uncapped samples, which exhibit a significant magnetic decay, as indicated by the aforementioned linear interpolation. Considering the capped samples, the average saturated magnetic moments were found to be approximately equal to $1.5 \cdot 10^{-4}$ emu, which indicates that the capping layer successfully protected the magnetic properties of the Permalloy film, which is a testament to the protective capabilities of the Al capping layer.

Considering the scattered values of m_S for the capped plasma samples, it would appear that the plasma-treated samples exhibit an increased saturated magnetic moment. From the presented XPS measurements, the capped plasma samples exhibited a chemically shifted signal in the Ni 2p spectrum in contrast to the metallic Ni signal obtained for the control and hotplate samples. The fact that the plasma sample deviates from the control and hotplate samples in both the Ni 2p spectra and in the VSM measurement insinuates that the slight increase in the saturated moment may be connected to the chemical shift. However, the increase is only of a minor character, on the order of 10^{-5} emu and thus

approaching the same order of magnitude as the system noise found in the noise assessment of the VSM module. Therefore, it is plausible that the increase of the saturated moment may be attributed to random noise of the VSM system rather than a true increase of saturated moment caused by the formation of an unidentified oxide compound.

At this stage, a discussion on the signal-to-noise ratio and its possible impact on the obtained results is due. Firstly, regarding the obtained values of m_S for the different experimental groups with a deposited metal thickness of 20 nm, the obtained signal is several orders of magnitude larger than the established RMSE of the VSM system. Additionally, the obtained values are used comparatively in assessing the relative magnitude of the magnetic moments; thus, random noise should not affect the results to any large extent. At the same time, the interpolation performed for samples with metal thicknesses of 10 nm was more prone to error due to a reduced signal-to-noise ratio. The average saturated moment of the uncapped 10 nm films was found to be $m_S = 6.7 \cdot 10^{-5}$ emu, yielding an appreciable signal-to-noise ratio of ~ 29, using the RMSE value obtained for the system noise. All the above considered, the noise of the VSM measurements is assumed to be of minor influence on the VSM results.

A final potential source of error in the VSM measurements which has not been addressed is batch-to-batch differences caused by the manual operation of the electron beam evaporator during metal deposition. The shutter which terminates the metal deposition was controlled manually, which means that a delayed or premature closing of the shutter would cause small deviations in the amount of deposited metal. However, having used a deposition rate of approximately one angstrom per second means that the deviation of deposited metal should be at most on the order of one angstrom. Considering the estimated oxide thickness of the uncapped control samples of $t_{\mathrm{Oxide}} = 1.1 \mathrm{nm}$, a deviation in actual metal thickness of 0.1 nm can be regarded as significant.

5.4 Implications of oxidation on Permalloy structures

Having presented the individual parts of the experimental results, the loss of the magnetic moment of the uncapped samples can be connected to the decrease of the metallic signal in the Ni 2p and Fe 3p XPS spectra. The curve fitted Ni 2p spectra indicated that the most prominent species of the oxide forming on a Permalloy surface are antiferromagnetic NiO and ferrimagnetic $NiFe_2O_4$ and Fe_3O_4. In that regard, it is plausible that the oxide contributes to the saturated magnetic of the samples. Firstly, the ferrimagnetic compounds can be regarded as weak ferromagnets, which will contribute to the total magnetic

moment of the sample. Concerning the NiO, the AF species have a nonzero magnetic susceptibility; however, the literature suggests that a field strength of approximately 5 T is required to switch the magnetic moments of NiO, which greatly exceeds the field strengths used in this work [43]. Therefore it is reasonable to assume that contribution to the saturated magnetic moment from NiO is negligible.

In the work of Fitzsimmons et al., the authors claim that the oxide forming on uncapped Permalloy is weakly ferromagnetic with a magnetization of less than 105 $\mathrm{kA\,m^{-1}}$ or equivalently 105 emu/cm^3 [36]. Comparing the average saturation magnetization, $M_\mathrm{S} = m_\mathrm{S}/V$, of 785 emu/cm^3 for the capped control samples measured in this work, the formation of the oxide amounts to a decay of magnetization approximately equal to 87% compared to the magnetization of the pure metal. This value resonates with the above discussion of a possible contribution from magnetic oxides to the saturated moment. An estimated decay of 87% also implies that the estimated oxide thicknesses can be regarded as conservative estimates, which might explain the discrepancy in the reported oxide thickness of 1.8 nm in the work of Mattera et al. versus the estimated thickness of 1.1 nm found for the control sample in this work [28].

At the same time, Mattera and coworkers reported an oxide thickness of 2.9 nm for the plasma oxygen plasma-treated samples which is smaller than the values obtained in this work. Albeit, the sample treatment performed in the aforementioned work was of a gentler nature than the one performed in this work, as the plasma samples were subject to oxygen plasma for two minutes at 32 W and 30 sccm. In comparison, having treated the samples for 30 minutes at 1000 W and 600 sccm would presumably cause a greater degree of oxidation which explains the discrepancy in the reported oxide thicknesses.

Having performed XPS measurements shortly after the fabrication of the respective batches, potential over-time effects for a timespan longer than three weeks can not be accounted for in this work. Therefore, performing XPS and VSM measurements on samples over a prolonged period could provide useful information about the nature of the oxidation rate of the uncapped Permalloy and potentially reveal the self-termination of the oxidation reaction due to an effective blocking of the reactants through the oxide scale.

At this stage, a discussion on the relevance and implications of the various sample treatments is in place. Firstly, it is highly implausible that an ASI or other magnetic structure will be exposed to extreme oxidizing environments comparable to the plasma cleaner or a hotplate. However, the sample treatments proved effective in producing an appreciable difference between the different experimental groups facilitating the discussion. Accordingly, the control samples represent the most relevant experimental group when assessing the implications

on ASI structures. It is worth emphasizing that an appreciable degree of oxidation was found for the uncapped control samples with an estimated oxide thickness of 1.1 nm. Considering the assumption regarding the formation of a non-magnetic oxide, the true oxide thickness may be assumed to take a value closer to 1.8 nm, as reported by Mattera et al. [28]. Although an appreciable decay of saturated magnetic moment was found for the circular disk samples, the implications on the magnetic behavior of the samples are assumed to be small. However, for a nanomagnet, this picture might change due to the increased surface-to-volume ratio at the nanoscale.

a) Kagome ASI   (b) Single nanomagnet
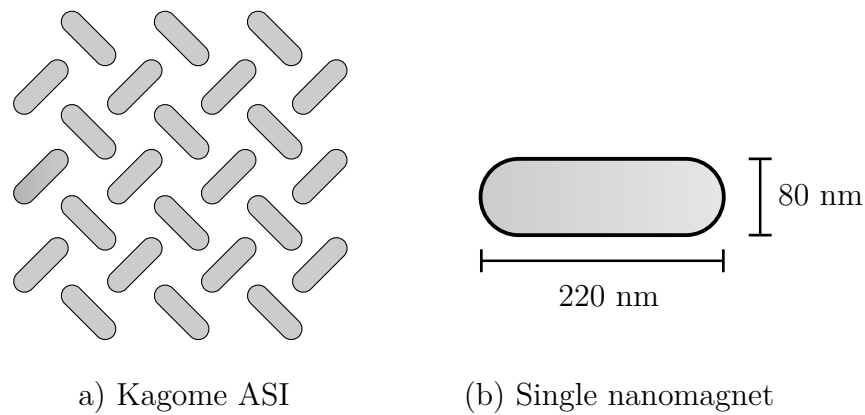
Figure 5.11: (a) Schematic of a kagome artificial spin ice and (b) a single stadium-shaped nanomagnet, comprising the ASI, with indicated sample dimensions.

Revising the scaling laws from first year nanotechnology curriculum, the surface to volume ratio of a system in terms of a characteristic dimension, D, increases for miniaturized systems: Surface/Volume $\propto D^{-1}$ [44]. Assuming an oxide scale with a thickness of 1.1 nm forms on the unprotected sidewalls of a stadium-shaped nanomagnet with dimensions 220 nm$\times$80 nm, shown schematically in figure 5.11, the fraction of oxide volume over the total volume amounts to approximately 4%. Conversely, using the stated oxide thickness of 1.8 nm from the literature, the fraction of consumed metal due to oxide formation equals approximately 6%. Both the calculated fractions are relatively small and suggest that even though an oxide layer forms on the sidewalls of a nanomagnet, the implications on the magnetic characteristics of the nanomagnet should be small to negligible.

6 | Conclusion

Through this work, the protective capabilities of Aluminum films as effective oxidation barriers have been confirmed, indicated by a persistent saturated magnetic moment of aluminum capped samples subjected to various experimental treatments. Another testament to the protective nature of the capping layer was found from a well-defined metallic nickel signal obtained in XPS measurements for the samples subjected to hot baking and the ambient atmosphere. On the other hand, the XPS measurements of the capped samples subjected to oxygen plasma revealed possible internal oxidation of the underlying metal indicated by a chemically shifted signal in the Ni 2p spectrum. Nevertheless, despite the severe sample treatment, the saturated magnetic moment of the plasma-treated samples was sustained.

Regarding the uncapped samples, a significant magnetic decay was found for all the experimental groups with a loss of saturated magnetic moment of approximately 8% between the uncapped and capped control samples. Chemical analysis of the samples suggested that antiferromagnetic NiO and ferrimagnetic $NiFe_2O_4$ and Fe_3O_4 represented the predominant species in the oxide forming on an unprotected Permalloy surface, which agrees with the observed loss of magnetic moment. Conservative estimates of the oxide thickness for the various experimental groups yielded a maximum of 3.1 nm obtained for the plasma-treated samples versus 1.1 nm for the control samples.

Magnetic measurements of capped and uncapped samples yielded an appreciable magnetic anisotropy, indicated by hard and easy axis magnetization curves for different sample orientations. The analysis of the TEM images suggested that the observed magnetic behavior could be ascribed to an anisotropy in the grain structure of the sample, as curve fits performed on the FFTs of TEM images with a resolved grain structure yielded high eccentricity ellipses, corresponding to a broken symmetry in the Fourier space. Considering that the Fourier transform reflects the symmetry of the original TEM image, the results suggest a structural anisotropy in the Permalloy film.

When it comes to the implications of oxidation on nanomagnets constituting ASI systems, the effect of an oxide layer forming on the sidewalls of the magnetic structures is assumed to be of minor significance. Additionally, the observed anisotropy of the circular samples used in this work is relatively weak compared to the shape anisotropy of the elongated nanomagnets used in artificial spin ices. However, the effects of oxidation on unprotected Permalloy surfaces on a longer time scale have not been accounted for, which may affect the magnetic characteristics of the structures to a greater extent.

Further Work

Given the limited time available to conduct the thesis, several topics fell outside the scope of the work, which may be pursued in the future.

Although the obtained results indicate that the magnetic Permalloy structures are able to sustain their magnetic characteristics over a short period, the effects of oxidation on a longer timescale are not accounted for and could potentially yield new insight into the oxidation reaction's kinetics and the material's resulting magnetic behavior. Additionally, the implications of Permalloy oxidation on artificial spin ice systems could be measured directly by performing similar experimental treatments on an ASI followed by magnetic characterization.

Lastly, employing alternative magnetic characterization techniques such as a magneto-optical Kerr magnetometer could potentially aid in unraveling the source of the magnetic anisotropy found in the Permalloy thin films.

References

[1] Moore, G. E. et al. (1965). *Cramming more components onto integrated circuits.*

[2] Natarajan, S. et al. (2014). "A 14nm logic technology featuring 2 nd-generation finfet, air-gapped interconnects, self-aligned double patterning and a 0.0588 μm 2 sram cell size". *2014 IEEE international electron devices meeting.* IEEE 3–7.

[3] Kim, N. S. et al. (2003). "Leakage current: Moore's law meets static power". *computer* 36 (12) 68–75.

[4] Pop, E., Sinha, S., and Goodson, K. E. (2006). "Heat generation and transport in nanometer-scale transistors". *Proceedings of the IEEE* 94 (8) 1587–1601.

[5] Jensen, J. H., Folven, E., and Tufte, G. (2018). "Computation in artificial spin ice". *ALIFE 2018: The 2018 Conference on Artificial Life.* MIT Press 15–22.

[6] Skjærvø, S. H. et al. (2020). "Advances in artificial spin ice". *Nature Reviews Physics* 2 (1) 13–28.

[7] Marković, D. et al. (2020). "Physics for neuromorphic computing". *Nature Reviews Physics* 2 (9) 499–510.

[8] Coey, J. M. (2010). *Magnetism and magnetic materials.* Cambridge university press.

[9] Kittel, C. (2021). "Introduction to solid state physics Eighth edition".

[10] Blundell, S. (2003). *Magnetism in condensed matter.*

[11] Zumdahl, S. S. and DeCoste, D. J. (2012). *Chemical principles.* Cengage Learning.

[12] Lyng-Jørgensen, J. (2021). *Hysteresis Design using Tailored Anisotropy in Artificial Spin Ice Systems.* Project report in TFE4570. Department of Electronic Systems, NTNU – Norwegian University of Science and Technology.

[13] Rinaldi-Montes, N. et al. (2016). "Size effects on the Néel temperature of antiferromagnetic NiO nanoparticles". *AIP advances* 6 (5) 056104.

[14] Kozioł-Rachwał, A. et al. (2022). "Beating the limitation of the Néel temperature of FeO with antiferromagnetic proximity in FeO/CoO". *Applied Physics Letters* 120 (7) 072404.

[15] O'handley, R. C. (2000). *Modern magnetic materials: principles and applications.* Wiley.

[16] Lawless, K. R. (1974). "The oxidation of metals". *Reports on Progress in Physics* 37 (2) 231.

[17] Hüfner, S. (2013). *Photoelectron spectroscopy: principles and applications.* Springer Science & Business Media.

[18] Foner, S. (1996). "The vibrating sample magnetometer: Experiences of a volunteer". *Journal of applied physics* 79 (8) 4740–4745.

[19] Einstein, A. (1905). "Über einem die Erzeugung und Verwandlung des Lichtes betreffenden heuristischen Gesichtspunkt". *Annalen der physik* 4.

[20] Chung, Y.-W. and Chung, Y. (2001). "Fundamental concepts in ultrahigh vacuum, surface preparation, and electron spectroscopy". *Practical guide to surface science and spectroscopy. Elsevier* 1–22.

[21] Chastain, J. and King Jr, R. C. (1992). "Handbook of X-ray photoelectron spectroscopy". *Perkin-Elmer Corporation* 40 221.

[22] Als-Nielsen, J. and McMorrow, D. (2011). *Elements of modern X-ray physics.* John Wiley & Sons.

[23] Major, G. H. et al. (2020). "Practical guide for curve fitting in x-ray photoelectron spectroscopy". *Journal of Vacuum Science & Technology A: Vacuum, Surfaces, and Films* 38 (6) 061203.

[24] Hesse, R. et al. (2013). "Comparative study of the modelling of the spectral background of photoelectron spectra with the Shirley and improved Tougaard methods". *Journal of Electron Spectroscopy and Related Phenomena* 186 44–53.

[25] Foner, S. (1959). "Versatile and sensitive vibrating-sample magnetometer". *Review of Scientific Instruments* 30 (7) 548–557.

[26] Fairley, N. et al. (2021). "Systematic and collaborative approach to problem solving using X-ray photoelectron spectroscopy". *Applied Surface Science Advances* 5 100112.

[27] McIntyre, N. and Zetaruk, D. (1977). "X-ray photoelectron spectroscopic studies of iron oxides". *Analytical Chemistry* 49 (11) 1521–1529.

[28] Mattera, M. et al. (2015). "Self-Assembled monolayers on a ferromagnetic permalloy surface". *Langmuir* 31 (19) 5311–5318.

[29] Wood, J. et al. (2018). "Control of ferromagnetic properties of Ni80Fe20 thin films by voltage-induced oxidation". *Journal of Applied Physics* 124 (8) 085304.

[30] Biesinger, M. C. et al. (2011). "Resolving surface chemical states in XPS analysis of first row transition metals, oxides and hydroxides: Cr, Mn, Fe, Co and Ni". *Applied Surface Science* 257 (7) 2717–2730.

[31] Gonzalez, R. C. and Wintz, P. (1987). *Digital Image Processing*. Addison Wesley.

[32] *Thermo Scientific XPS* (n.d.). `https://www.jp.xpssimplified.com/elements/aluminum.php`. Accessed: 2022-05-27.

[33] Gorobez, J., Maack, B., and Nilius, N. (2021). "Growth of Self-Passivating Oxide Layers on Aluminum—Pressure and Temperature Dependence". *physica status solidi (b)* 258 (5) 2000559.

[34] Jeurgens, L. et al. (2002). "Growth kinetics and mechanisms of aluminum-oxide films formed by thermal oxidation of aluminum". *Journal of applied physics* 92 (3) 1649–1656.

[35] Biesinger, M. C. et al. (2009). "X-ray photoelectron spectroscopic chemical state quantification of mixed nickel metal, oxide and hydroxide systems". *Surface and Interface Analysis: An International Journal devoted to the development and application of techniques for the analysis of surfaces, interfaces and thin films* 41 (4) 324–332.

[36] Fitzsimmons, M., Silva, T. J., and Crawford, T. (2006). "Surface oxidation of Permalloy thin films". *Physical Review B* 73 (1) 014420.

[37] Yamashita, T. and Hayes, P. (2008). "Analysis of XPS spectra of Fe2+ and Fe3+ ions in oxide materials". *Applied surface science* 254 (8) 2441–2449.

[38] Schwertmann, U. and Cornell, R. M. (2008). *Iron oxides in the laboratory: preparation and characterization*. John Wiley & Sons.

[39] Smith, D. O. (1959). "Anisotropy in permalloy films". *Journal of applied physics* 30 (4) S264–S265.

[40] Park, E. B. et al. (2012). "Induced magnetic anisotropy and strain in permalloy films deposited under magnetic field". *Thin solid films* 520 (18) 5981–5984.

[41] Prosen, R., Holmen, J., and Gran, B. (1961). "Rotatable anisotropy in thin permalloy films". *Journal of Applied Physics* 32 (3) S91–S92.

[42] Langørgen, A. (2020). "Magnetic Force Microscopy and Micromagnetic Simulations of Nanoscale Magnetic Structures and Modified Artificial Spin Ices". MA thesis. NTNU.

[43] Moriyama, T. et al. (2018). "Spin torque control of antiferromagnetic moments in NiO". *Scientific reports* 8 (1) 1–6.

[44] Rogers, B., Adams, J., and Pennathur, S. (2007). *Nanotechnology: understanding small systems*. Crc Press.

A | List of fabricated samples

Table A.1: List of fabricated samples and a description of their experimental purposes.

Sample composition	Description
20 nm Permalloy + 2.5 nm Aluminum	Standard Al capping fabricated in two batches. Subjected to the various experimental treatments and measured in VSM and XPS.
10 nm Permalloy	Subjected to the various experimental treatments to determine oxide thickness from VSM measurements.
20 nm Permalloy	Uncapped Py film fabricated in two batches. Subjected to the various experimental treatments and measured in VSM and XPS.
40 nm Permalloy	Subjected to the various experimental treatments to determine oxide thickness from VSM measurements.

B | XPS scan parameters

Table B.1: List of the XPS parameters used in the various XPS scans.

Scan name	Mode	Pass energy [eV]	Dwell time [ms]	ΔE [eV]
Wide scan	FAT	160	100	1
O 1s	FAT	20	332	0.1
C 1s	FAT	20	260	0.1
Ni 2p	FAT	20	162	0.1
Fe 3p	FAT	20	199	0.1
Al 2p	FAT	20	298	0.1
Si 2p	FAT	20	397	0.1

C | XPS curve fitting parameters

Table C.1: Curve fitting parameters used in Ni 2p$_{3/2}$ spectra.

Sample	Peak number (from the left)	Associated compound	Peak binding energy [eV]	FWHM [eV]	Area [%]
Control	1	NiO	861.1	2.86	13.3
	2	Ni satallite	858.5	2.60	6.2
	3	NiO	855.3	3.100	46.3
	4	NiO	853.7	0.96	2.9
	5	Ni metal	852.5	1.05	31.2
Hotplate	1	NiO	861.3	3.66	20.3
	2	Ni satallite	858.7	2.38	2.7
	3	NiO	855.3	3.29	53.0
	5	Ni metal	852.7	0.97	19.4
	6	NiFe$_2$O$_4$	854.4	1.26	4.7
Plasma	1	NiO	861.2	4.51	35.6
	2	NiO	855.5	3.03	58.0
	6	NiFe$_2$O$_4$	854.4	1.03	6.4
Batch 1	1	NiO	861.1	3.67	17.5
	2	NiO	855.4	3.09	57.1
	3	Ni metal	852.5	0.92	23.8

Table C.2: Curve fitting parameters used in Al 2p spectra.

Sample	Peak number (from the left)	Associated compound	Peak binding energy [eV]	FWHM [eV]	Area [%]
Control	1	Al_2O_3	74.8	1.39	75.4
	2	AlO_x	858.5	2.60	6.2
	3	Al $2p_{1/2}$	72.4	0.54	6.0
	4	Al $2p_{3/2}$	72.0	0.64	12.1
Hotplate	1	Al_2O_3	74.4	1.43	81.1
	2	AlO_x	72.8	1.62	6.8
	3	Al $2p_{1/2}$	72.1	0.48	4.0
	4	Al $2p_{3/2}$	71.7	0.56	8.1
Plasma	1	Al_2O_3	74.4	1.73	100.0

Table C.3: Curve fitting parameters used in Fe 3p spectra.

Sample	Peak number (from the left)	Associated compound	Peak binding energy [eV]	FWHM [eV]	Area [%]
Control	1	Fe_2^+, Fe_3^+	55.3	2.81	32.1
	2	Fe	52.7	1.62	67.9
Hotplate	1	Fe_2^+, Fe_3^+	55.5	3.19	84.4
	2	Fe	52.8	1.34	15.6
Plasma	1	Fe_2^+, Fe_3^+	55.5	2.89	100.0
Batch 1	1	Fe_2^+, Fe_3^+	55.1	3.31	84.9
	2	Fe	52.5	1.1	15.1

D | X-ray physics nomenclature

Table D.1: Quantum numbers and their respective X-ray physics and spectroscopic notations.

Quantum numbers				Spectroscopic notation	X-ray notation
n	l	s	j		
1	0	$\pm 1/2$	1/2	$1s_{1/2}$	K
2	0	$\pm 1/2$	1/2	$2s_{1/2}$	L_1
2	1	$-1/2$	1/2	$2p_{1/2}$	L_2
2	1	$+1/2$	3/2	$2p_{3/2}$	L_3
3	0	$\pm 1/2$	1/2	$3s_{1/2}$	M_1
3	1	$-1/2$	1/2	$3p_{1/2}$	M_2
3	2	$+1/2$	3/2	$3p_{3/2}$	M_3
3	2	$-1/2$	3/2	$3d_{3/2}$	M_4
3	2	$+1/2$	5/2	$3d_{5/2}$	M_5
$\vdots$	$\vdots$	$\vdots$	$\vdots$	$\vdots$	$\vdots$

E | Script for TEM image processing

```python
1   #General imports
2   import cv2
3   import numpy as np
4   from matplotlib import pyplot as plt
5   from skimage import data
6   from skimage.filters import threshold_multiotsu
7   import os
8   os.chdir(directory)
9
10  # Reading TEM image from file
11  image_filename = "TEM_W3_TR_cropped.png"
12  image = cv2.imread(image_filename)
13
14  # Creating gaussian blur mask
15  height, width = image.shape[:2]
16  x_gauss = cv2.getGaussianKernel(width,180)
17  y_gauss = cv2.getGaussianKernel(height,180)
18
19  kernel = x_gauss * y_gauss.T
20  mask = kernel * 255 / np.linalg.norm(kernel)
21
22  # Applying gaussian blur to TEM image and saving vignette
23  output = np.copy(image)
24  output[:,:,0] = image[:,:,0] * mask
25  output[:,:,1] = image[:,:,1] * mask
26  output[:,:,2] = image[:,:,2] * mask
27  cv2.imwrite('TEM_W3_TR_cropped_vignette.png', output)
28
29  # Helper function performing 2D Fourier transform
30  def fft_2D(input):
31      ft = np.fft.ifftshift(input)
32      ft = np.fft.fft2(ft)
33      return np.fft.fftshift(ft)
34
35
36
```

```
37      # Plotting and saving the FFT
38      fig, axs = plt.subplots()
39      image = plt.imread('TEM_W3_TR_cropped_vignette.png')
40
41      # Converting to grayscale
42      image = image[:, :, :3].mean(axis=2)
43      plt.set_cmap("gray")
44      ft = fft_2D(image)
45      axs.imshow(np.log(abs(ft)))
46      axs.axis("off")
47      plt.savefig('FFT_W3.png', format = 'png')
48      plt.title('FFT')
49      plt.show()
50
51      # Applying contrast enhancment, CLAHE, and saving result
52      fft = cv2.imread('FFT_W3.png', 0)
53
54      clahe = cv2.createCLAHE(clipLimit=2.0, tileGridSize=(8,8))
55      fft_enhanced = clahe.apply(fft)
56      cv2.imwrite('FFT_W3_CLAHE.png', fft_enhanced)
57
58      # Applying multi-Otsu threshold generating 5(6) classes
59      # and plotting for visualization
60      img = cv2.imread('FFT_W3_CLAHE.png', 0)
61      thresholds = threshold_multiotsu(img[img != 0], 6, 256)
62      regions = np.digitize(img, bins=thresholds)
63
64      fig, axs = plt.subplots(nrows=1, ncols=2, figsize = (10,5))
65
66      # Plotting the FFT image.
67      axs[0].imshow(img, cmap='gray')
68      axs[0].set_title('CLAHE enhanced FFT')
69      axs[0].axis('off')
70
71      # Plotting the Multi Otsu result.
72      axs[1].imshow(regions, cmap='jet')
73      axs[1].set_title('Multi-Otsu thresholds')
74      axs[1].axis('off')
75
76      plt.subplots_adjust()
77      plt.show()
78
79      # Selecting relevant thresholds for generating binary mask
80      relevant_thresh = thresholds[-3:-1]
81
82      # Detecting contours and fitting ellipses
83      cList = []
84      rList = []
85      img = cv2.imread('FFT_W3_CLAHE.png', 0)
86
87
```

```
88      for threshold in relevant_thresh:
89          # Generating binary mask
90          ret, thresh = cv2.threshold(img, threshold, 255,
91          cv2.THRESH_BINARY)
92
93          # Detecting contours of binary
94          contours, hierarchy = cv2.findContours(thresh,
95          cv2.RETR_LIST, cv2.CHAIN_APPROX_SIMPLE)
96
97          for i in range(len(contours)):
98              if len(contours[i]) < 5: continue
99
100             # Fitting ellipse to contour
101             rrt = cv2.fitEllipse(contours[i])
102             perimeter = cv2.arcLength(contours[i],True)
103
104             # Saving correctly fitted ellipses
105             if perimeter > 200 and perimeter < 1500:
106                 cList.append(contours[i])
107                 rList.append(rrt)
108             x, y = rrt[0]
109
110     for i in range(len(rList)):
111         if len(rList) != 0:
112             (x,y),(MA,ma),angle = cv2.fitEllipse(cList[i])
113
114             # Adding ellipse onto FFT image
115             e = cv2.ellipse(img, rList[i], (255, 255, 255),
116              1, cv2.LINE_AA)
117             a = ma/2
118             b = MA/2
119         else: print('Perimeter restrictions to strict')
120         eccentricity = np.sqrt(pow(a,2)-pow(b,2))
121         eccentricity = round(eccentricity/a,2)
122         if angle != 90.0:
123             # Printing eccentricity and angle of orientation
124             # for fitted ellipse
125             print('Eccenticity %i: '%i,eccentricity,
126             '\nTheta : ', angle)
127
128     # Saving curve fitted FFT
129     cv2.imwrite("FFT_W3_curveFit.png", img)
130
```

Listing E.1: Script for TEM image processing